Final draft for *Applied Optics*

May 6, 1993

Comparison of numerical models for computing underwater light fields

Curtis D. Mobley

Jet Propulsion Laboratory

California Institute of Technology

Mailstop 300-323

4800 Oak Grove Drive

Pasadena, California 91009

Bernard Gentili

Laboratoire de Physique et Chimie Marines

Université Pierre et Marie Curie

F06230 Villefranche-sur-Mer, France

Howard R. Gordon

Physics Department

University of Miami

Coral Gables, Florida 33124

Zhonghai Jin
Geophysical Institute
University of Alaska
Fairbanks, Alaska 99701

George W. Kattawar
Physics Department
Texas A&M University
College Station, Texas 77843

André Morel
Laboratoire de Physique et Chimie Marines
Université Pierre et Marie Curie
F06230 Villefranche-sur-Mer, France

Phillip Reinersman
Marine Science Department
University of South Florida
St. Petersburg, Florida 33701

Knut Stamnes
Geophysical Institute
University of Alaska
Fairbanks, Alaska 99701

Robert H. Stavn
Biology Department
University of North Carolina
Greensboro, North Carolina 27412

Abstract

Seven models for computing underwater radiances and irradiances by numerical solution of the radiative transfer equation arc compared. The models arc applied to the solution of several problems drawn from optical oceanography. The problems include highly absorbing and highly scattering waters, scattering by molecules and by particulates, stratified water, atmospheric effects, surface wave effects, bottom effects, and Raman scattering. The models provide consistent output with errors (owing to Monte Carlo statistical fluctuations) in computed irradiances being seldom larger, and usually smaller, than the experimental errors made in measuring irradiances when using current oceanographic instrumentation. Computed radiances display somewhat larger errors,

I. Introduction

Various numerical models arc now in usc for computing underwater irradiances and radiance distributions. These models were designed to address a wide range of oceanographic problems. The models arc based on various simplifying assumptions, have differing levels of sophistication in their representation of physical processes, and employ several different numerical solution techniques.

In spite of the increasingly important roles these numerical models arc playing in optical oceanography, the models remain incompletely validated in the sense that their outputs have not been extensively compared with measured values of the quantities they predict. This desirable mode]-data comparison is not presently possible because the requisite comprehensive oceanic optical data sets arc not available. Such data sets must contain simultaneous measurements of the inherent optical properties of the sca water (e.g. the absorption and scattering coefficients, and the scattering phase function), environmental parameters (e.g. the sky radiance distribution and sca state) and radiometric quantities (e.g. the complete radiance distribution, or various irradiances). The inherent optical properties and the environmental parameters arc needed as input to the numerical models; the radiometric variables arc the quantities predicted by the models. Current developments in oceanic optical instrumentation and measurement methodologies give cause for hope that data sets adequate for comprehensive model-data comparisons will become available within the next fcw years.

Meanwhile, our faith in these models' predictions rests upon careful debugging of computer code, on internal checks such as conservation of energy or known relations between inherent and apparent optical properties, on simulation of a fcw grossly simplified situations for which analytical solutions of the radiative transfer equation arc available, and on comparison (sometimes indirect) with incomplete data sets. An additional worthwhile check on the various models can bc made by applying them to a common set of realistic problems. Such model-model comparisons help to identify errors in coding or weakensses in the mathematical representation of physical phenomena, to quantify numerical errors particular to the various solution algorithms, to determine optimum numerical techniques for simulation of particular physical phenomena, and to determine which models might bc appropriate for inclusion in a future library of underwater radiative transfer codes corresponding to those now available for atmospheric radiative transfer modeling (such as LOWTRAN[1]).

In March 1991, the Oceanic Optics Program of the Office of Naval Research sponsored a workshop in order to foster a close examination of the various models now in use, and in order to begin the process of model-model comparison. This paper reports the results of that comparison. The models being evaluated arc described in Sec. II. During the workshop the participants defined a set of canonical (standard) problems for usc in model comparisons. These problems arc documented in Sec. 111. Section IV presents selected results obtained when the models of Sec. 11 are applied to the problems of Sec. 111.

1 I. Numerical Models

All of the numerical models compared here generate an approximate solution to the time-independent, monochromatic radiative transfer equation in onc spatial dimension:

$$\mu \frac{\partial L(\tau;\mu,\phi)}{\partial \tau} = -L(\tau;\mu,\phi) + \omega_o(\tau) \int\int_{(\mu',\phi')\in\Xi} L(\tau;\mu',\phi')\, \tilde{\beta}(\tau;\mu',\phi' \to \mu,\phi) d\mu' d\phi' + S(\tau;\mu,\phi). \quad (1)$$

Here $L(\tau;\mu,\phi)$ is the unpolarized spectral radiance (at wavelength λ, omitted for brevity) at optical depth τ and in direction (μ,ϕ), ω_o is the scattering-to-attenuation ratio, $\tilde{\beta}$ is the scattering phase function, and S represents any internal source of radiance, The depth τ is measured positive downward from the mean sea surface, and the polar angle $\theta = \cos^{-1}\mu$ is measured from the nadir direction. (See Tab. I for a list of symbols, their units and definitions.) In order to solve Eq. (1) within a water body, it is necessary to specify (1) the inherent optical properties of the water body, ω_o and $\tilde{\beta}$, (2) the distribution of internal sources S, (3) the radiance distribution externally incident on the boundaries of the water body, and (4) the physical nature of the boundaries themselves.

The models differ primarily in the mathematical techniques used to solve Eq. (1) and in the treatment of boundary conditions at the sca surface. Two of the models described below (models 11 and DO) employ analytical (invariant imbedding and discrete ordinates) techniques for solving Eq. (1), and five of the models (MC 1-MC5) employ probabilistic (Monte Carlo) techniques. Each of the models, as applied to the solution of the canonical problems defined in Sec. 111, solves Eq. (1) for a plane-parallel water body that is laterally homogeneous but may be inhomogeneous with depth. The upper boundary of the water body is the wind-blown, random air-sea interface. The lower boundary is either an infinitely thick layer of water below the greatest depth of interest, or an opaque reflecting bottom at a finite depth. The models all assume that externally applied radiance is incident downward on the upper side of the air-water surface. The models are all monochromatic and there arc no internal sources of radiance (such as bioluminescence). However, some of the models can simulate inelastic scattering processes by sequential solutions of Eq. (1). For example, the model is first run at the wavelength of excitation, λ_{ex}, to compute the energy shifted by inelastic scattering from λ_{ex} to another wavelength λ, and then the model is run again at λ, with the radiance shifted from λ_{ex} appearing as a source term S at λ. A particular example of S used in this treatment of Raman scattering is given in the Appendix. The models all account for multiple scattering and can usc realistic scattering phase functions that arc highly peaked in forward directions, as is the case for sca water.

Several of the models have additonal capabilities, such as the computation of polarized radiance in the Stokes vector format and the simulation of azimuthally anisotropic random air-water surfaces. These capabilities arc not evaluated in this paper.

All but one of the models directionally discretizes Eq. (1) by partitioning the set of all directions, Ξ, into a grid of quadrilateral regions bounded by lines of constant μ and constant ϕ, plus two polar caps (collectively called "quads"). The fundamental quantity computed by these models is the quad-averaged radiance defined by

$$L(\tau;u,v) \equiv \frac{1}{\Omega_{uv}} \int \int_{(\mu,\phi)\in Q_{uv}} L(\tau;\mu,\phi)\, d\mu\, d\phi. \tag{2}$$

$L(\tau;u,v)$ is physically interpreted as the average radiance over the set of directions (μ,ϕ) contained in the uv^{th} quad, Q_{uv} (u labels μ bands and v labels ϕ bands), which subtends a solid angle of size Ω_{uv}. In the model comparison wc chose to usc 24 Q-bands of uniform width $\Delta\phi = 15°$, and 20 p-bands of size $\Delta\mu = 0.1$. However, a polar cap with $\Delta\mu = 0{,}1$ has a half-angle of $\theta = 25.8°$, which is much larger than onc would normally usc in computing nadir or zenith radiances. Therefore, some models were run with a slightly different μ spacing and smaller polar caps. The remaining model (DO) computes the radiance $L(\tau;\mu,\phi)$ in particular (μ,ϕ) directions.

Wc now briefly describe the distinguishing features of the various models.

Model II (Invariant Imbedding, author C. D. M.) The integral operator of Eq. (2), which averages any quantity over the set of directions $(\mu,\phi) \in Q_{uv}$, can be applied to Eq. (1). The result is a quad-averaged radiative transfer equation in which $L(\tau;\mu,\phi)$ is replaced by $L(\tau;u,v)$, integration over all directions is replaced by summation over all quads, and the phase function $\tilde{\beta}(\tau;\mu',\phi'\rightarrow\mu,\phi)$ is replaced by a quad-averaged quantity $\tilde{\beta}(\tau;r,s\rightarrow u,v)$ that specifies how much of the radiance initially headed into quad Q_{rs} gets scattered into quad Q_{uv}. Using standard techniques of Fourier analysis and invariant imbedding theory, the equations for the $L(\tau;u,v)$ are transformed into a set of Riccati differential equations governing the depth dependence of certain reflectance and transmittance functions within the water body. Depth integration of the Riccati equations (by a high-order Runge-Kutta algorithm) and incorporation of the boundary conditions at the sea surface and bottom leads eventually to the desired $L(\tau;u,v)$ at all depths. These mathematical operations are outlined in Mobley[2] and are described in full in Mobley and Preisendorfer[3]. The inherent optical properties of the water body can vary arbitrarily with depth, Absorption and scattering are built up as sums of terms representing the contributions by pure water, particles of various types, and dissolved substances.

This model uses a Monte-Carlo simulation of the wind-blown sea surface to evaluate certain quad-averaged, bi-directional reflectance and transmittance functions that describe how the sea surface reflects and transmits radiance incident on the surface from above and below. In this simulation, the sea surface is resolved into a grid of triangular wave facets whose vertex elevations are randomly determined from any chosen wave slope-wind speed spectrum in a manner described in Mobley and Preisendorfer[3] and in Preisendorfer and Mobley[4]. The surface simulation allows for multiple reflections of rays by wave facets and for the possibility of shadowing of one facet by another. The probabilistic ray-tracing calculations for setting up the surface boundary conditions are independent of the analytical computations within the water body. Moreover, since the ray tracing involves only the surface wave facets, for which it is assumed that there is no absorption, no rays are "lost" to absorption. It is therefore computationally feasible to trace a sufficient number of rays to reduce the Monte Carlo fluctuations in the computed bi-directional surface functions to a negligible level.

This model docs not include an atmosphere *per se*. The sky radiance incident on the sea surface is obtained either from an analytic model (e.g. a cardioidal distribution, or the empirical model of Harrison and Coombes[5]), or from the output of a separately run atmospheric radiative. transfer model . In the simulation of problem 4, below, LOWTRAN-7 was run to generate the sky radiance at the center of each of the μ-ϕ quads; that value was then taken as the average sky radiance over the quad.

The bottom boundary can be either an infinitely thick homogeneous layer of water below some depth τ_{max}, or an opaque bottom at τ_{max}. in the infinite-depth case, the hi-directional radiance reflectance properties of the infinite layer below τ_{max} arc obtained from an eigenmatrix analysis described in Preisendorfer[6]. The same analysis yields the asymptotic diffuse attenuation coefficient k_∞ and the asymptotic radiance distribution $L_\infty(\mu)$ appropriate for the homogeneous layer. In the opaque-bottom case, the reflectance properties of the bottom are explicitly specified, for example as a lambertian surface with a given irradiance reflectance.

The chief advantage of this model is computational efficiency. Solution of the Riccati differential equations for L is an analytic process, and thus there arc no Monte Carlo fluctuations in the computed radiances (except for a negligible amount introduced by the simulation of the sea surface). In particular, both upwelling and downwelling radiances are computed with the same accuracy. Moreover, computation time is a linear function of depth, so that accurate radiance distributions arc easily obtained at great depths ($\tau > 10$). Computation time depends only mildly on quantities such as the scattering-to-attenuation ratio, surface boundary conditions, and water stratification. The associated computer code is available and is documented in Mobley[7].

Model DO (Discrete Ordinates, authors Z.J. and K. S.) This model solves Eq. (1) directly" without applying the quad-averaging implied by Eq. (2). The radiance is expanded into a Fourier cosine series, $L(\tau,\mu,\phi) = \sum_{m=0}^{2N-1} L^m(\tau,\mu)\cos(\phi-\phi_o)$, and the phase function into a series of $2N$ Legendre polynomials,

$$\tilde{\beta}(\tau;\mu',\phi'\rightarrow\mu,\phi) \equiv \tilde{\beta}(\tau;\cos\psi) = \sum_{l=0}^{2N-1} (2l + 1)\, g_l(\tau)\, P_l(\cos\psi) ,$$

where $g_l(\tau)$ is the expansion coefficient and ψ is the scattering angle. The advantage of these expansions is that the azimuthal dependence is isolated in the sense that $2N$ independent equations for the Fourier coefficients $L^m(\tau,\mu)$ arc obtained:

$$\mu\frac{dL^m(\tau,\mu)}{d\tau} = - L^m(\tau,\mu) + \omega_o(\tau)\int_{-1}^{1} L^m(\tau,\mu')\beta^m(\tau;\mu',\mu)\, d\mu' + s^m(\tau,\mu) ,$$

where

$$\beta^m(\tau;\mu',\mu) = \frac{1}{2}\sum_{l=m}^{2N-1} (2l + 1)\, g_l(\tau)\, \frac{(l - m)!}{(l + m)!}\, P_l^m(\mu)\, P_l^m(\mu') .$$

Here $P_l^m(\mu)$ is the associated Legengre polynomial,

The atmosphere and the ocean arc divided into a suitable number of layers to adequately resolve the optical properties of each of the two media. Each layer is taken to bc homogeneous, but the optical properties arc allowed to vary from layer to layer, (For a homogeneous medium, only onc layer is required.) At the interface between the ocean and the atmosphere (assumed to bc flat), Fresnel's formula is used to compute the appropriate reflection and transmission coefficients, and Snell's law is applied to account for the refraction taking place there.

The integral term in each of these azimuth-independent equations is then approximated by a Gaussian quadrature sum using $2N_1$ terms ("streams") in the atmosphere and $2N_2$ terms in the ocean, so that there arc $2N_1$ streams in the refractive region of ocean that "communicate" directly with the atmosphere, and $2N_2 - 2N_1$ streams in the total reflection region of the ocean, In this way the- intcgro-differential equation is transformed into a system of coupled ordinary differential equations that is solved by the discrete ordinate method, as described in more detail elsewhere[8], subject to appropriate boundary conditions at the top of the atmosphere and the bottom of the ocean, The basic discrete ordinate method used here is described and thoroughly documented in previous publications[9-11]. The modifications required to apply the method to a system consisting of two adjacent media with different indices of refraction arc described by Jin and Stamnes[8].

This method has the following unique features, (i) Because the solution is analytic, the computational speed is completely independent of individual layer and total optical thickness, which may be taken to be arbitrarily large. The computational speed is directly proportional to the number of horizontal layers used to resolve the optical properties in the atmosphere and ocean. (ii) Accurate irradiances arc obtained with just a few streams, which makes the code very efficient. (iii) Because the solution is analytic, radiances and irradiances can be returned at arbitrary optical depths unrelated to the computational levels. (iv) The DO method is essentially a matrix eigenvalue-eigenvector solution, from which the asymptotic solution is automatically obtained, The smallest eigenvalue is k_∞, and the associated eigenvector is L_∞.

Desirable and possible extensions of the method include (i) the computation of inelastic scattering effects to treat phenomena such as Raman scattering, and (ii) the inclusion of a wind-blown surface to simulate the basic features of sea surface roughness. These extensions would require some modifications of the existing computer code.

Model MC1 (Monte Carlo 1, author H. R. G.) This model simulates radiative transfer in both the ocean and the atmosphere, as coupled across a wind-roughened interface. The code is designed to simulate irradiances as a function of depth for computation of the irradiance reflectance E_u/E_d and diffuse attenuation functions such as $K_d = -d(\ln E_d)/dz$. The nadir-viewing radiance L_u is also computed as a function of depth for the computation of $Q = E_u/L_u$. The optical properties of the ocean arc continuous] y stratified in the vertical. They can be specified as discrete values as a function of depth (with linear interpolation between the given depths) or determined from formulas as in problem 3, below. Separate scattering phase functions arc used for the particles and for the water itself. Variants of this code have been used for a number of studies of radiative transfer in the ocean[12-17].

The sea surface roughness is modeled using the Cox and Munk[18] surface slope distribution for a given wind speed. The effect of the surface roughness is not simulated exactly because the possibility of shadowing of onc facet by another is ignored. Multiple scattering, however, is included: e.g. if a downward-moving photon in the atmosphere encounters the sea surface and is still moving downward after reflection, it will undergo a second interaction with the sca surface, Onc important aspect of this model is the proper usc of photon weights to account for the fact that not all facets arc oriented in such a manner as to be able to interact with an incident photon, i.e. facets with normals making an angle less than 90° to the direction of the incident photon. The sequence of events during an interaction with the surface follows. From Cox and Munk, the probability that the x and y components of the surface slope, z_x and z_y respectively, arc within $z_x \pm ½dz_x$ and $z_y \pm ½dz_y$ is

$$p(z_x,z_y)\ dz_x\ dz_y = \frac{1}{\pi\sigma^2} \mathrm{Cxp}\left(-\frac{z_x^2 + z_y^2}{\sigma^2}\right) dz_x\, dz_y\,,$$

or

$$p(\theta_n,\phi_n)\ d\theta_n\ d\phi_n = \frac{1}{\pi\sigma^2} \exp\left(-\frac{\tan^2\phi_n}{\sigma^2}\right) \tan\phi_n \sec^2\phi_n\, d\theta_n\, d\phi_n\,,$$

where

$$\sigma^2 = 0.003 + 0.00512\ u\ .$$

Here U is the wind speed in m s"], ϕ_n is the angle between the normal to the facet and the normal to the level surface, and θ_n is the azimuth of the normal. Given random numbers ρ_θ and ρ_ϕ on the unit interval (0,1), the model finds θ_n and ϕ_n from

$$\theta_n = 2\pi\rho_{\theta_n}$$

$$\rho_{\phi_n} = \frac{1}{2\pi^2\sigma^2} \int_0^{\phi_n} \exp\left(-\frac{\tan^2\phi_n'}{\sigma^2}\right) \tan\phi_n' \sec^2\phi_n'\ 64\$,,'.$$

The photon interacting with the surface is given the weight

$$w = \frac{\cos\omega \sec\phi_n}{\iint_{\cos\omega>0} p(z_x,z_y)\ \cos\omega \sec\phi_n\, dz_x\, dz_y},$$

where ω is the angle of incidence on the chosen facet. The weight W accounts for sampling from $p(z_x,z_y)$ even though all facets arc not visible to the photon.

The atmospheric part of the mode] consists of fifty, one-kilometer layers with both molecular and aerosol scattering. The vertical distribution of the optical properties is taken from Elterman[19]. The aerosol phase function at the given wavelength is determined from Mic theory[20] using Deirmendjian's Haze C size distribution[21]

$$\frac{dn(r)}{dr} \propto \frac{1}{r^{\nu+1}},$$

where r is the particle radius, $h(r)$ is the number of particles pcr unit volume with radius between r and $r + dr$; $\nu = 3$ is used in the computations. The aerosol total scattering coefficient at each altitude is proportional to λ^{-P}, where $P = \nu - 2$; however $P \approx 0.75$ fits Eltermans's data better. When a photon interacts with the atmosphere, the scattering angle is chosen from either the molecular or aerosol phase functions based on the ratio of their scattering coefficients for the layer in which the interaction takes place.

When inelastic processes arc to be included, the above code is operated at the excitation wavelength λ_{ex} to determine the excitation radiance distribution, This is used as input to a second Monte Carlo code that computes the light field at the wavelength of interest[17]. As with the elastically scattered radiation, the goal is to determine the irradiances of the inelastically scattered radiation, This is a considerable simplification because the solution can be effected by working with the azimuthally averaged radiance at λ, i.e. only the azimuthally averaged radiative transfer equation need be solved. The details of this formulation arc given in the Appendix.

Model MC2 (Monte Carlo 2, author G. W. K,) This model also simulates a coupled ocean-atmosphere system. The Monte Carlo code relics heavily on several variance reducing schemes to increase computational efficiency. Wc give only a brief description of onc of the most useful ones. The use of statistical weights allows us to treat each photon history as a *packet* of photons rather than as a single photon. Photons arc never allowed to escape from the ocean-almosphcrc systcm. The method of forced collisions is used, whereby wc sample from a biased distribution that ensures a collision along the path, and the weight is then adjusted appropriately to unbias the result, The way this is done is as follows. Suppose onc wants to compute the expectation value $\langle f \rangle$ of some function f of a random variable x, using a probability density function $p(x)$. By definition,

$$\langle f \rangle = \int f(x)\, p(x)\, dx\,.$$

However, if wc want to sample from the density function $\tilde{p}(x)$ then

$$\langle f \rangle = \int f(x)\, \frac{p(x)}{\tilde{p}(x)}\, \tilde{p}(x)\, dx = \int f(x)\, w(x)\, \tilde{p}(x)\, dx\,,$$

where $w(x) \equiv p(x)/\tilde{p}(x)$ is called the statistical weight. The variance σ^2 of $f(x)w(x)$ when sampling from the biased distribution is given by

$$\sigma^2[f(x)\, w(x)] = \int \left[f(x)\, w(x) - \langle f \rangle\right]^2 \tilde{p}(x)\, dx\,.$$

Although this method appears straightforward, it dots have pitfalls. If the weight can have values that exceed unity, then one can have a variance that far exceeds the variance in the unbiased sampling. Therefore, extreme caution must bc used when using this method. It should be noted that this is a very powerful method for studying perturbation effects, bccausc several processes can bc simultaneously emulated with the same set of photon histories.

Now consider the tcchniquc of forced collisions, in which photons arc never allowed to escape the medium. Let τ_b denote the optical path length to a boundary. To insure that the photon never escapes, wc sample the path length according to the probability density function

$$\tilde{p}(\tau)\, d\tau = \frac{e^{-\tau}\, d\tau}{1 - e^{-\tau_b}}\,, \qquad 0 \le \tau \le \tau_b\,.$$

The weight now has to bc multiplied by $[1 - \exp(-\tau_b)]$ to remove the bias. It should bc noticed that this factor is always lcss than unity and should produce a smaller variance than when using unforced sampling. Histories arc terminated only when the statistical weight falls below some specified valuc.

When an interaction occurs, the packet weight is multiplied by the single scattering albedo ω_o, which gives the fraction of photons that can continue to scatter. The level air-water interface is modeled by using the appropriate Fresnel reflection and transmission coefficients. A random number is chosen at this stage to determine whether the photon is transmitted or reflected.

Radiances are obtained over detectors that have finite solid angles. However, statistical estimation can be used to give true continuum radiance values where no directional averaging is done. This model can simulate inelastic scattering; the details arc given in Kattawar and Xu[22], The Monte Carlo method has also been extended to include the full Stokes vector treatment of polarization[23-26]; these papers show that substantial errors can occur if polarization is neglected.

Model MC.? (Monte Carlo 3, authors A.M. and B. G.) This Monte Carlo model is similar to those described in Plass and Kattawar[27,28] and in Gordon and Brown[29]. It is designed to simulate the radiance distribution at any level in the atmosphere and in the ocean. Between these two media, a wind-roughened interface is modeled using the isotropic Gaussian distribution of sca surface slopes, as discussed under model MC1. The probability of occurrence of the various slopes is modified when considering nonvertically incident photons. This photon-facet interaction is modeled as in Plass, *et al.*[30]; it does not account for the possible occultation of a facet by an adjacent one. Transmitted and reflected photon packets resulting from interaction with the air-water surface arc weighted according to Fresnel's law (including the possibility of total internal reflection), According to the problem under investigation, photon packets arc introduced at the top of the atmosphere, or just above (or below) the ocean surface. For specific problems involving deep levels, packets can be rc-introduced at intermediate depths inside the water body, according to a directional distribution that reproduces the downward radiance field as resulting from a previous Monte Carlo run, The bottom boundary is either an infinitely thick absorbing layer, in which photons arc lost from the system, or a lambertian reflecting bottom of a given albedo, from which weighted photon packets are reflected.

After each collision, the weight of each photon packet is multiplied by the local value of ω_o pertinent to the altitude or the depth, to account for its partial absorption. A packet history is terminated when its weight falls below a predetermined value, typically 1 xl 0^{-6}. For each collision a random number on the unit interval is compared to the local value of the ratio of the. molecular scattering coefficient to the total scattering coefficient, to determine if the scattering, event will be of molecular type (air or water molecules), or due to an aerosol or hydrosol particle, The appropriate phase function is then used to determine the scattering angle; the orientation of the scattering plane is chosen at random on the interval $(0,2\pi)$. The number of photons initiated depends on the single-scattering albedo value, so as to control the stochastic noise in the computed radiometric quantities (details can be found in Morel and Gentili[31,32]). The model is operated for its oceanic segment with the optical properties as specified in Sec. 11 I. For the atmospheric segment, fifty 1-km thick layers arc considered, with specified values for Rayleigh and aerosol scattering and for ozone absorption as in Elterman[19]. The aerosol phase function (as computed by Mic scattering theory) for the maritime aerosol model defined by the Radiation Commission of IAMAP is used; see the models of Tanré, *et al.*[33] and Baker and Frouin[34].

Model MC4 (Monte Carlo 4, author P.R.) This model is intended primarily for simulation of the radiance distribution above and just below the surface, and for simulation of irradiances with the first five mean free paths of the surface. The model is based on techniques described by Kirk[35]. The model atmosphere is composed of fifty layers, each characterized by separate Rayleigh and particulate scattering coefficients and an albedo of single scattering, as given by Elterman[19]. Weighted photon beams arc projected into the atmosphere from the atmosphere-space boundary, and a collision is forced somewhere in the atmosphere along this original trajectory. The attenuated beam, which is the weight of the original beam less the portion lost to scattering and absorption, strikes the sea surface at the angle of the original trajectory. Beam losses due to absorption and scattering take place at the point of collision. There the absorbed portion is lost and the scattered portion exits the collision point in another single, weighted beam. A random number is' compared to the ratio of the Rayleigh scattering cross section to the total scattering cross section to determine the type of volume scattering function governing the scattering event. In the case of an aerosol scattering, a two-term Henyey-Greenstein phase function is used to determine the scattering angle[36]. Otherwise, the angle is determined by a Rayleigh phase function[37]. Once the trajectory of the scattered portion of the beam is calculated, the distance from the point of collision to the next encountered interface (air-water or air-space) is determined. A new collision is forced somewhere along this trajectory, and the process is repeated until the weight of the scattered portion of the beam falls below a preset minimum fraction of the original beam weight. This minimum traceable weight is set to 1x10-6 of the original beam weight for the simulations presented below.

Some of the scattered trajectories encounter the atmosphere-space boundary and are forgotten; the others impinge on the sea surface. For the latter, the angle of incidence depends on the nadir angle of the ray and slope of the sea surface. The directions of the reflected and refracted rays are determined geometrically, and the weights of the rays are calculated from the Fresnel formula. Although wave shadowing is neglected, multiple surface interactions may occur. A reflected ray that is still projected downward, or a transmitted ray projected upward, must encounter the sea surface again immediately, without an intervening trajectory. Ray trajectories resulting from reflection are followed in the original manner. Transmitted portions of the beams are followed similarly until encountering the bottom or the sea surface, or until being diminished to less than the minimum traceable weight, Those beams striking the bottom are lost; those incident upon the sea surface from below are again subjected to the reflection and transmission calculations, *Model MC5* (Monte Carlo 5, author R. H. S.) The Naval Research Laboratory (NRL) optical model (referred to as the NORDA or NOARL optical model in earlier publications) uscs standard Monte Carlo tcchniqucs[13,28,35]. At each scattering event, a random numbcr is used to dctcrminc if the scattering is duc to molecular water, quartzlikc particulatcs, algae, or organic detritus; the volume scattering functions of these components arc treated separately, rather than using an average volume scattering function. The model includes the effects of Raman scattcring. If a photon collision results in inelastic scattering (as dctcrmincd by comparing a random number to the appropriate optical propcrtics of the medium), the wavelength is shifted by an amount corresponding to the mean wavcnumbcr shift of 3357 cm^{-1} corresponding to Raman scatter by water molcculcs. The finite bandwidth of the Raman-shiftcd light is taken into account by averaging over 10 rim-bandwidths (roughly corresponding to current oceanographic instruments); details of this averaging arc dcscribcd in Stavn and Wcidcmann[38,39]. For the simulation of problcm 7, below, it was assumed that the Raman scattering occurs in a very narrow wavcband. The photons arc tallied into zonal bands, as is convenient for computation of irradianccs and the nadir-viewing radiance.

There is no atmosphere *per se* implcmcntcd in the model. Atmospheric transmittances of solar irradiancc needed for simulations arc obtained from the non-layered atmospheric model of Brinc and Iqbal[40]. The mode] dctcrmincs the skylight radiance pattern from the empirical mode] of Harrison and Coombcs[5]. The present version of the code handles only homogeneous waters.

111. Canonical Problems

Wc now define several canonical, or standard, problems for solution by undcrwatcr radiative transfer models. Models claiming to provide realistic simulations of the oceanic optical environment should bc able to solve these problems, and provide output that is at least as accurate as the data obtainable by presently available instrumentation. In brief, these problems arc

Problcm 1: An unrcalistically simplc problcm

Problcm 2: A *base problem* using realistic inherent optical properties for the sea water

Problem 3: The base problcm, but with stratified water

Problcm 4: The base problcm, but with atmospheric effects

Problcm 5: The base problcm, but with a wind-blown sca surface

Problem 6: The base problcm, but with a finite-depth bottom

Problcm 7: A problcm involving Raman scattering.

In each of these problems, the water body is taken to bc horizontally homogeneous. The real index of refraction of the water is n = 1.340. The depth below the surface can bc specified by either the nondimensional optical depth τ or by the geometric depth z in meters. The base problcm 2 assumes that (1) the air-water surface is flat, (2) the water is homogeneous and infinitely deep, (3) there is no atmosphere, i.e. the sky is black, (4) the sun is a point light source located at a zenith angle of θ_{sun} = 60°, (5) the sun provides a spectral irradiance just above the sca surface of magnitude $E_{\perp}$ = 1 W m^{-2} ri^{m-}] on a surface perpendicular to the sun's rays (which gives E_d = 0.5 W m^{-2} rim-l for θ_{sun} = 600), (6) there is no inelastic scattering or other sources of light within the water body, (7) the angular scattering properties of the water arc characteristic of natural hydrosols, and (8) the water is either highly scattering (ω_o = 0.9) or highly absorbing (ω_o = 0.2). The other problems arc defined by exceptions to these assumptions. The specific problcm definitions arc as follows.

Problem 1. A Raylcigh phase function

$$\tilde{\beta}_w(\mu',\phi' \rightarrow \mu,\phi) \equiv \tilde{\beta}_w(\psi) = \frac{3}{16\pi}(1 + \cos^2\psi) \tag{3}$$

is used to dcscribc the angular scattering properties of the water. The scattering angle ψ is related to the incident (p',$') and scattered ($\mu,\phi$) directions by

$$\psi = \cos^{-1}\left[\mu\mu' + \sqrt{1-\mu^2}\sqrt{1-\mu'^2}\cos(\phi - \phi')\right]$$

This phase function, which is plotted in Fig. 1(b) below, is similar to that of pure sea water. The Rayleigh phase function is a well behaved function of the scattering angle ψ and presents no numerical difficulties in its treatment; wc therefore consider this an "easy" problem for numerical modeling. Note that $\tilde{\beta}_w$ satisfies the normalization

$$2\pi \int_0^\pi \tilde{\beta}(\psi) \sin\psi \, d\psi = 1. \tag{4}$$

Both highly scattering ($\omega_o = 0.9$) and highly absorbing ($\omega_o = 0.2$) cases arc considered for the Rayleigh phase function.

Problem 2. This "base" problem uses a phase function that is typical of oceanic waters. The total volume scattering function (VSF) β is

$$\beta = \beta_w + \beta_p ,$$

where subscripts w and p refer to pure sca water and to particles, respectively. The total phase function $\tilde{\beta}$ therefore can bc expressed as

$$\tilde{\beta} = \frac{b_w}{b}\tilde{\beta}_w + \frac{b_p}{b}\tilde{\beta}_p . \tag{5}$$

This total $\tilde{\beta}$ must satisfy the normalization (4), which is the case if $\tilde{\beta}_w$ and $\tilde{\beta}_p$ arc each normalized.

The particle phase function $\tilde{\beta}_p$ is defined from three VSF'S measured by Petzold[41] in San Diego Harbor. The VSF for pure sca water[42] was first subtracted to find the three particle VSF's. Then the scattering coefficient of pure sea water[43] (b_w = 0,00231 m^{-1} at λ = 530 nm, the wavelength of Petzold's data) was subtracted from the respective scattering coefficients computed by Petzold (b = 1.205, 1.536, and 1.824 m^{-1} for the three VSFs) to find the particle scattering coefficient b_p for each VSF. The three particle phase functions were then computed using these b_p's, and the mean value of the three $\tilde{\beta}_p$'s was computed at each scattering angle, This mean $\tilde{\beta}_p(\psi)$ becomes infinite at ψ = O, if it is assumed that $\tilde{\beta}_p(\psi) - \psi^{-m}$ as $\psi \rightarrow 0$, where m = 1.346 is the negative of the slope of $\log \tilde{\beta}_p(\psi)$ vs. $\log \psi$ at the two smallest tabulated scattering angles (ψ = 0.10° and O. 125890). When this functional form of $\tilde{\beta}_p$ was used to analytically integrate $2\pi \tilde{\beta}_p(\psi)\sin\psi$ from ψ = O to ψ = 0.10°, and the trapezoidal rule was used to integrate from ψ = 0.12589° to ψ = 180°, the normalization integral (4) gave the value 1.006449. Wc thus divided the mean $\tilde{\beta}_p$ by 1.006449 to obtain the values shown in Tab. II. The. particle phase function $\tilde{\beta}_p(\psi)$ is then *defined* to bc the tabulated values, with linear interpolation to bc used between the tabulated values, and with $\tilde{\beta}_p(\psi) \equiv \tilde{\beta}_p(0.\ 12589°)(0.\ 12589°/\psi)^{1.346}$ for ψ < 0.12589°, The resulting $\tilde{\beta}_p(\psi)$ is defined for all ψ and exactly satisfies the normalization condition (4). This $\tilde{\beta}_p$ is plotted in Fig. 1(b), below.

Moreover, since b_w = 0.00231 m^{-1} is much less than b_p (> 1.2 m^{-1} for each of the Petzold VSF's), it is reasonable to neglect the contribution of the water, $\tilde{\beta}_w$, to the total phase function of Eq (5). This omission creates an error of at most a fcw percent in $\tilde{\beta}$ even at backscattered directions (ψ > 900). Wc therefore define the total phase function for problem 2 to bc just the particle phase function as defined above: $\tilde{\beta}(\psi) \equiv \tilde{\beta}_p(\psi)$. This $\tilde{\beta}$ is representative Of phase functions measured in ocean waters with typical particle concentrations and, because of its highly peaked behavior at small ψ, can bc expected to test the numerical models' abilities to handle realistic phase functions. Both highly scattering and highly absorbing cases arc considered for this phase function.

Problem 3. This problem is designed to test the models' abilities to compute light fields in highly stratified water. The water stratification is specified as follows. The particulate absorption and scattering coefficients arc taken to bc

$$a_p = 0.04\ C^{0.602} \tag{6a}$$

and

$$b_p = 0.33\, C^{0.620}, \tag{6b}$$

respectively, where C is the chlorophyll (pigment) concentration. When C is in mg m^{-3}, a_p and b_p are in m^{-1}. The absorption representation (6a) is based on Prieur and Sathyendranath[44] at a wavelength of λ = 500 nm, The scattering representation (6b) is based on Gordon and Morel[45] with λ = 500 nm and assuming that $b_p(\lambda) \sim \lambda^{-1}$. The pigment profile with depth is based on Lewis, *et al.*[46] and consists of a gaussian plus a constant background:

$$c(z) = C_o + \frac{h}{s\sqrt{2\pi}} \exp\left[-\frac{1}{2}\left(\frac{z - z_{max}}{s}\right)^2\right]. \tag{7a}$$

Platt and Sathyendranath[47] show that Eq. (7a) with the parameter values

$$C_O = 0.2 \text{ mg m}^{-3} \tag{7b}$$

$$s = 9 \text{ m} \tag{7c}$$

$$z_{max} = 17 \text{ m} \tag{7d}$$

$$h = 144 \text{ mg m}^{-2} \tag{7e}$$

fits data from the Celtic Sea in May very well. We therefore adopt Eq. (7) as a reasonable model for C(z). When Eq. (7) is used in Eq. (6), the particulate absorption and scattering coefficients, and hence all inherent optical properties, become functions of depth. The absorption and scattering coefficients for pure sea water at λ = 500 nm are given by[43]

$$a_w = 0.0257 \text{ m}^{-1} \tag{8a}$$

and

$$b_w = 0.0029 \text{ m}^{-1}. \tag{8b}$$

When the chlorophyll concentration is low, scattering by pure sea water makes a significant contribution to the total scattering at large scattering angles (almost ½ when C = CO and ψ = 1800). Therefore, for this problem it is necessary to use Eq. (5) to determine the total phase function from the phase functions for pure sea water, $\tilde{\beta}_w$, and for particles, $\tilde{\beta}_p$, as were defined in problems 1 and 2. The phase function is now a function of depth, as is the scattering-to-attenuation ratio

$$\omega_o \equiv \frac{b}{c} = \frac{b_w + b_p(z)}{a_w + a_p(z) + b_w + b_p(z)} \text{"}$$

Figure 1(a) shows *a, b, c* and ω_o as functions of depth for problem 3, and Fig. 1(b) shows the phase functions at selected depths.

Problem 4. This problcm is the same as problcm 2 with $\omega_o = 0.9$, except that atmospheric effects are included. The sky is no longer black, but rather has a radiance distribution that describes the atmosphere's scattering and absorption effects on sunlight, The incident solar irradiance, $E_\perp = 1$ W m^{-2} ri^{m-}], is now applied at the top of the atmosphere. The atmospheric optical effects arc defined by Elterman's[19] aerosol and Rayleigh scattering optical thicknesses at $\lambda = 500$ nm:

$$\tau_{aerosol} = 0.264$$

$$\tau_{Rayleigh} = 0.145.$$

Since the numerical models incorporate atmospheric effects in various ways, a more detailed specification of the atmosphere is not made.

Problem 5. This problem is the same as problem 2 with $\omega_o = 0.9$, except that the effects of a wind-blown sca surface arc included. The surface waves arc statistically specified as having a wave slope standard deviation of $\sigma = 0.2$ in the Cox-Munk[18] capillary wave spectrum

$$\sigma^2 = 0.003 + 0.00512\, U\ ;$$

where *U is* the wind speed in meters pcr second. Thus $\sigma = 0.2$ corresponds to a wind speed of $U = 7.23$ m s^{-1}. The solar zenith angle is taken to be $\theta_{sun} = 80°$.

Problem 6. This problem is the same as problem 2, except that a finite-depth bottom is imposed. The bottom is taken to be an opaque, lambertian reflecting surface at depth $\tau = 5$. This surface has an irradiance reflectance (E_u/E_d) of 0.5. Such a surface is a reasonable model of a light colored, sandy bottom.

Problem **7,** This problcm is for usc in comparing models that include the effects of Raman scattering by water molcculcs. The wavelength of excitation is taken to bc λ_{ex} = 417 nm, and all light that is Raman scattcrcd at 417 nm is assumed to shift to λ = 486 nm. Thc Raylcigh phase function, Eq. (3), is used for elastic scattering. The phase function for Raman scattering is[48]

$$\beta_{Ram}(\psi) = \frac{3}{16\pi}\frac{1+3\rho}{1+2\rho}\left(1+\frac{1-\rho}{1+3\rho}\cos^2\psi\right), \tag{9}$$

where ρ is the dcpolarization ratio. For this problcm, wc usc p = 0.17 and take the total Raman scattering coefficient b_{Ram} equal the elastic scattering coefficient of the water itself, i.e. $b_{Ram} = b_w$. The absorption and elastic scattering coefficients of pure sca water at the wavelengths in question as taken from Smith and Bakcr[43] are

$$a_w(417) = 0.0156 \text{ m}^{-1}$$
$$b_w(417) = 0.0063\ m``$$
$$a_w(486) = 0.0188\ m`*$$
$$b_w(486) = 0.0032\ m^{-1}.$$

Considering the way in which Smith and Baker inferred a_w from irradiance data, it is assumed that b_{Ram} is already included in the value of a_w. Thus the total beam attenuation coefficient at each wavelength is just $a_w + b_w$. A unit irradiancc $E_\perp$ is incident at the sca surface on a plane normal to the solar beam at the excitation wavelength λ_{ex} =41 7 nm. There is no atmosphere and no solar irradiancc is incident on the sca surface at λ = 486. The resulting irradianccs at 486 nm arc those that would bc duc solely to inelastic scattering from 417 nm. The solar zenith angle is 60° and the air-water surface is flat,

Table III summarizes the various canonical problems,

IV. Model Comparisons

Although the models generally compute the radiance L, the quantities most often used in oceanic optics arc various irradiances. These irradiances arc defined by weighted integrations of the radiance distribution over the upward and downward hemispheres of directions, as shown in Tab. 1, and are easily obtained from computed radiances. The nadir-viewing radiance L_u is the radiance seen by a sensor pointed straight down (in the nadir direction); L_u is important in remote sensing studies. The ability of a numerical model to accurately compute the irradiances and nadir radiance is a measure of its utility for many oceanographic studies.

Models 11 and DO compute all quantities with equal accuracy. However, the Monte Carlo models MC1-MC5 compute upwelling quantities (e.g. E_u, E_{ou}, or L_u) with less accuracy than downwelling quantities (e.g. E_d or E_{od}). This is because most of the simulated photons, all of which are initially heading downward, continue to head downward and thereby contribute to E_d or E_{od}. However, only the relatively fcw photons that arc scattered into upward directions can contribute to E_u, E_{ou}, or L_u; fewer photons means greater statistical fluctuations in the computed values.

Also, for a given initial number of photons, the Monte Carlo models must settle for lcss accuracy at a given optical depth τ in highly absorbing waters (small ω_o) than in highly scattering waters (large ω_o). This is because photons absorbed before they reach depth τ are not available to bc tallied in the computation of the radiance or irradiance, whereas scattered photons can eventually reach depth τ and bc tallied. In practice, the accuracy of the Monte Carlo models is strongly dcpcndcnt on the number of photon collisions; thus more photons must bc processed when ω_o is small, in order to achieve satisfactory accuracy. The accuracy of models 11 and DO is independent of ω_o.

With the above comments in mind, wc selected E_d, E_{ou} and L_u for comparison just above the sca surface and at τ = 1, 5 and 10. Problems 1 and 2 have both highly scattering (ω_o = 0.9) and highly absorbing (ω_o = 0,2) waters, Although it is not possible to compare the computational efficiencies of the various models because they were run on a variety of computers, with differing numbers of photons traced in the Monte Carlo codes, Tab. IV shows some representative execution times. It should be noted that the long execution times shown for some of the Monte Carlo codes arc the times required for accurate radiance simulations at large depths. If only irradiances or near-surface radiances arc required for a particular study, these models can be run for much shorter times. For example, in the simulation of problem 3, output from model MCI was compared for run times of 180 s and 7200 s, The E_d values throughout the euphotic zone (roughly the upper 21 m), as accumulated after 180 s, were within 1.5% of the values obtained after 7200 s. After 180 s, the E_{ou} and L_u values just below the surface (at z = O) were within 1 % of their final values. Deeper within the euphotic zone, E_{ou} and L_u differed by as much as 8% and 20%, respectively, for the two run times. At a depth of z =60 m, the differences in the computed quantities for the two times were 3% for E_d, 19% for E_{ou}, and a factor of six for L_u. Model DO is much more efficient for irradiance than for radiance computations, because only the azimuthally averaged equation (i.e. the m = O component of the radiance) is required to compute irradiances or azimuthally averaged radiances. Full radiance computations require the evaluation of additional azimuthal components, Strongly anisotropic scattering also requires a large number of streams.

We now briefly discuss the results of the models' simulations of problems 1-7.

Problem 1. Figure 2(a) shows the computed E_d, E_{ou} and L_u for the Rayleigh phase function of problem 1 and ω_o = 0.9. In this and subsequent figures, we plot the results from the two analytic models, Il and DO, with solid lines; the Monte Carlo results arc plotted with dashed lines. This makes it easy to scc that, in most instances, the Monte Carlo results arc distributed to either side of the analytic results, which arc usually indistinguishable in the figures.

We first note in Fig. 2(a) that all models predict nearly the same values for a given quantity, although there is a detectable spread in L_u values owing to Monte Carlo fluctuations. This behavior is expected, based on the preceeding discussion, However, we also note that all models predict nearly the same values for Ed and E_{ou}, which is counter to intuition based on oceanographic experience. This result is easily explained if we recall that the Rayleigh phase function is nearly isotropic (independent of the scattering angle) and that the medium is highly scattering. Because of the intense scattering, the incident collimated radiance distribution approaches its asymptotic form very quickly with depth. Preisendorfer[49] shows that for an isotropic phase function the asymptotic radiance distribution L_∞ has an elliptical shape:

$$L_\infty(\theta) = \frac{L_o}{1 + k_\infty \cos\theta} \quad \text{(lo)}$$

Here LO depends only on the inherent optical properties, and k_∞ *is* the eccentricity of the ellipse; k_∞ is numerically equal to the nondimensional asymptotic diffuse attenuation coefficient. The analytic forms of L_∞ for a Rayleigh phase function and a Rayleigh phase matrix are also known[50] For ω_o = 0.9 the Rayleigh L_∞ *is* very, c1osc to elliptical, and so wc can use the simpler form of Eq. (1 O) for the following argument. The E_d and E_{ou} corresponding to L_∞ of Eq. (1 O) arc

$$\begin{aligned} E_d &= -\frac{2\pi L_o}{k_\infty^2}\left[k_\infty + \ln(1 - k_\infty)\right] \\ E_{ou} &= \frac{2\pi L_o}{k} \ln(1 + k_\infty)\,. \end{aligned} \quad (11)$$

Now the value of k_∞ for the problem at hand turns out to be $k_\infty \approx 0.52$ (see Tab. VII, below). This value is coincidentally very near to the value k_∞ = **0.531,** which makes $E_d = E_{ou}$ in Eq. (11), thus explaining the numerical results seen in Fig. 2(a). This peculiar behavior of E_d and E_{ou} depends both on the phase function and on the scattering-to-attenuation ratio. Such behavior is not seen in the output for the other problems, nor would it ever be encountered in a natural water body.

Note also that both E_d and E_{ou} arc greater just below the water surface than just above it, which may also seem counterintuitive. However, this is just the phenomenon of "optical energy trapping" in highly scattering waters, as discussed by Stavn, *et al.*[51] and by Plass, *et al.*[52]. In the present case of a solar angle of 60°, more than 93% of the incident solar irradiance is transmitted through the level surface into the water. About one half of the highly diffuse upwelling irradiance just below the surface is reflected back down by the surface. The total ***Ed*** just below the surface is the sum of the transmitted solar contribution and the reflected upwelling contribution; this sum is greater than Ed(air). Likewise, E_{ou}(air) consists of the (relatively weak) specularly reflected solar beam plus diffuse light transmitted upward through the water surface; this sum is less than E_{ou} just below the surface,

Figure 2(b) shows the output for the Rayleigh phase function and a highly absorbing medium with $\omega_o = 0.2$. Now E_{ou} *is* an order of magnitude less than *Ed*. There is almost a factor-of-three spread in the Monte Carlo estimates of E_{ou} at $\tau = 10$, and three of the Monte Carlo models had too few photons left at $\tau = 10$ to provide an estimate of L_u at that depth. This behavior is expected for this highly absorbing case.

Table V displays the average (over all models) values of E_d, E_{ou} and L_u at selected depths for this and the remaining problems. These data arc provided for readers who wish to compare their own models with ours. Such comparisons should be especially worthwhile for simple parameterized models that attempt to compute irradiances without solving the complete radiative transfer equation. The table also displays the ratio of the sample standard deviation s to the sample mean $\bar{x}$,

$$\frac{s}{\bar{X}} = \frac{\left[\frac{1}{N-1}\sum_{i=1}^{N}(x_i - \bar{x})^2\right]^{1/2}}{\frac{1}{N}\sum_{i=1}^{N} x_i},$$

where xi is the result predicted by the i^{th} model for the quantity of interest, and N is the number of model predictions ($N = 7$ for most quantities). The ratio $s/\bar{x}$ is a quantitative measure of how close together the models' predictions arc for a given quantity. Inspection of this ratio for problem 1 shows that the model predictions arc usually closer together for the highly scattering case (ω_o = **0.9**) than for the highly absorbing case (ω_o = 0.2), closer together at shallow depths, and closest together for E_d. The greatest spread in values is for L_u at large depths, owing to the small number of photons available for its estimation by the Monte Carlo models.

Problem 2. Figure 3 shows the models' output for problem 2. Figure 3(a) is for the highly scattering case of ω_o = 0.9. Each of the seven models provides essentially the same values for E_d and for E_{ou} to 10 optical depths (and deeper); some Monte Carlo fluctuation is apparent in the L_u values. Figure 3(b) shows the same computations for the highly absorbing case of ω_o = **0.2.** Once again, all models give nearly the same values for E_d and for E_{ou} to 10 optical depths. Now, however, considerable Monte Carlo fluctuation in the L_u values is seen at even shallow depths; only models II, DO and MC3 were able to compute L_u below τ = 10.

We emphasize that the large fluctuations seen in some of the estimates in Fig. 3(b) are simply the result of tracing an insufficient number of photons in the simulations, and not of any inadequacies in the models themselves. Tracing additional photons, at a proportional increase in computational expense, can reduce these fluctuations to any desired level. The particular values seen in Fig. 3 are each the result of one simulation. Running the Monte Carlo models with different seeds for their random number generators would generate a noticeably different set of curves for those instances where large fluctuations are seen in Fig. 3. It should be noted that there are certain sampling schemes that can improve the statistics at greater depths. However, this improvement is usually at the expense of larger errors in the radiometric quantities at smaller depths.

The euphotic zone is the region of a water body where there is sufficient light for photosynthesis to take place. In normal daylight conditions, it extends from the surface to a depth where the irradiance is roughly one percent of its surface values, We see in Fig. 3(b) that E_d and E_{ou} have decreased by two orders of magnitude at about four optical depths. Each of the models produces nearly identical irradiances to depths greater than τ = 4, so that each of the models is perfectly adequate for the purposes of biological oceanography. Likewise, the models produce very nearly the same water-leaving radiances, L_u(air), as would be of interest in remote sensing studies.

Problem **3.** Figure 4 shows the models' output for problem 3, the stratified water case. The one-percent irradiance level is now at about z = 21 m. Once again, the models provide nearly identical output to depths far below the euphotic zone.

Problem 4. Figure 5 shows E_d values near the water surface for the simulation of problem 4, the case with an atmosphere. The different ways in which the models simulate the atmosphere lead to an 1896 spread in the values of E_d just above the water surface, This difference in Ed(air) values is then carried throughout the underwater computations. The $s/\bar{x}$ ratio displayed in Tab. V is uniformly large for this problem because of the systematic offset of the different models' predictions. Note that apparent optical properties, such as reflectances and diffuse attenuation functions, arc *not* affected by this offset, because the apparent properties arc defined as ratios of radiometric quantities. For example, the $s/\bar{x}$ ratio for the K_d values computed from the plotted E_d values at depths z = O and 1 m is 0.009, which is much smaller than the $s/\bar{x}$ = 0.076 value tabulated for E_d at τ = O.

Problem 5. Four of the models (II, MCI, MC3 and MC4) are capable of simulating a wind-blown air-water surface as defined in problem 5. Figure 6 shows output from these models for a solar zenith angle of θ_{sun} = 80°. The models arc nearly identical in their output, even in this case of nearly horozontal incidence, for which any differences in the models should be most noticeable. Note that E_{ou}(air) is greater than Ed(air). This is because E_{ou}(air) contains a large contribution by the specularly reflected solar beam: simulations by Preisendorfer and Mobley[4] show that the reflectance of a capillary-wave surface is greater than 0.22 for a wind speed of 7.23 m S-l and θ_{sun} = 80°. The solar beam contribution to E_d is weighted by a $\cos\theta_{sun}$ factor, which is small for θ_{sun} = 80°.

Problem 6. Models II, DO, and MC3 can simulate a finite-depth bottom. Figure 7 shows the output from both models for the case of ω_o = 0.2; the models arc clearly in excellent agreement. It is easy to show that E_{ou} = E_d for a lambertian surface of reflectance 0.5, and all three models show this expected result at depth τ = 5.

Problem 7. Four of the models (MCI, MC2, MC3 and MC5) can simulate Raman scattering. Table VI compares the inelastically scattered contributions to the downwelling and upwelling plane irradiances, E_d and E_u respectively, for the simulation defined in problem 7. The models are clearly in excellent agreement, even though their respective formulations of inelastic scatter are somewhat different.

Computation of radiance distributions. Five of the models (II, DO, MC2, MC3 and MC4) compute the full radiance distribution, rather than just tallying photons as necessary to compute the irradiances and L_u. Figure 8 illustrates the consistency with which the various models compute the radiance distribution. The figure shows $L(\tau,\theta,\phi)$ in the plane of the sun at depths of τ = O, 5 and 20 for problem 2, ω_o = 0.9. Direction (θ_v,ϕ_v) gives the *viewing* direction, i.e. the. direction an instrument points in order to detect photons traveling in the (θ = 180° – θ_v, $ = 180° + ϕ_v) direction. Thus θ_v = O corresponds to looking straight up and seeing photons heading, straight down; the nadir radiance L_u of Fig. 3(a) is the value plotted at θ_v = 180°. The sun is in the ϕ_v = 0° half-plane.

The curves of Fig. 8 arc explained as follows. Wc begin at τ = O (in the water just below the surface) with our backs to the sun (looking in the ϕ_v = 180° direction). Looking straight down wc scc the nadir radiance at (θ_v,ϕ_v) = (1 80°, 1800). Looking up toward the horizontal (ϕ_v = 900), the radiance increases slightly owing to total internal reflection of radiance that has been scattcrcd into nearly horizontal directions. The radiance then decreases quickly as our viewing angle passes beyond the critical angle for total internal reflection, $\theta_v \approx$ 48°. In the region around θ_v = 0° wc arc looking upward and seeing the upwelling radiance that is reflected downward by the level water surface. Note for example (using the digital output from Model 11) that $L(\tau{=}0,\theta_v{=}0°)/L(\tau{=}0,\theta_v{=}1\,80°)$ = 1.737 x104/8,236x10-s = 0.021, which is just the Fresnel reflectance of the surface for perpendicular incidence. Recall that in problem 2 the sky is black, so there is no sky radiance transmitted through the surface. In problem 4 (not shown), transmitted sky radiance "fills in" the large dip in the radiance near $\theta_v = 0^o$. As our view passes the zenith we are now facing the sun. The large spike in the radiance near $(\theta_v,\phi_v) = (40°,00)$ is the refracted solar beam, The noticeable Clv-offset in the position of the plotted peak radiance occurs because different models choose their quad boundaries differently. The "radiance values arc plotted at the θ_v values of the quad centers, which range from 40.3° to 45.0° for the quad containing the refracted solar beam; plotted points arc connected by straight lines. Passing beyond the sun, wc see a large horizontal radiance, which decreases as wc look downward.

Model DO shows a more pronounced "spike" in the radiance near the solar direction, and more pronounced changes near the 48° critial angle, than do the other models. This is because model DO computes radiances in specific directions, rather than quad-averaged radiances. The angular quadrature points in model DO arc clustered near the critical angle and near the horizon, in order to get increased resolution in regions where the radiance varies rapidly with polar angle.

By depth $\tau = 5$, scattering has "smeared out" the solar beam and increased the downwelling radiance seen when looking upward near the zenith. The radiance distribution at $\tau = 20$ is very similar in shape to the asymptotic distribution, $L_\infty(\theta_v)$. The asymptotic distribution as computed by model 11 and normalized to the largest value of $L(\tau=20)$ is shown as a dotted line in Fig. 8. Note that only a small amount of Monte Carlo fluctuation is seen even at $\tau = 20$, for this highly scattering case.

Radiance distributions computed by the various models are in equally close agreement for the other canonical problems (except for Monte Carlo fluctuations in the small-ω_o cases) and will not be discussed.

Computation of asymptotic radiances. The asymptotic radiance regime (also called the diffusion regime) is the region far enough from the boundaries of a homogeneous medium that the radiance is independent of the incident direction of the source and of boundary effects. Radiance in the asymptotic regime is independent of the azimuthal angle ϕ, and it decreases exponentially as $\exp(-k_\infty \tau)$. Here $k_\infty = K_\infty/c$, where K_∞ is the dimensional (in m^{-1}) asymptotic diffuse attenuation coefficient and c is the beam attenuation coefficient. The *shape* $L_\infty(\theta)$ of the asymptotic radiance distribution is determined only by the inherent optical properties of the water; it is independent of depth.

Model 11 computes $L_\infty(\theta)$ and the associated value of the nondimensional asymptotic diffuse attenuation coefficient k_∞ by the solution of a matrix eigenvalue equation[6]. The smallest eigenvalue of the matrix is k_∞, and the associated eigenvector gives L_∞. Model DO obtains the asymptotic solution in a similar fashion. Models MC2 and MC3 obtain L_∞ and k_∞ by solution of the equivalent integral equation[49,53]

$$(1 + k_\infty \mu)\, L_\infty(\mu) = \omega_o \int_0^{2\pi}\int_{-1}^{1} L_\infty(\mu')\, \tilde{\beta}(\psi)\, d\mu'\, d\phi' . \tag{12}$$

The exact anal ytical solution to Eq. (12) for the case of scattering according to a Rayleigh phase function, as well as for a Rayleigh phase matrix, was found by Kattawar and Plass[50]. Numerical solutions for phase functions that arc highly peaked in the forward direction have been given in Kattawar and Plass[50] and in Prieur and Morel[w].

Figure 9 shows the computed $L_\infty(\theta_v)$, normalized to one at $\theta_v = 0°$, for problems 1 and 2, The numerical results are in excellent agreement for problem 2 and for the $\omega_o = 0.9$ case of problem 1, which also agrees with its exact analytic solution. However, the numerical results differ considerably for the $\omega_o = 0.2$ case of problem 1, and each is considerably off from the analytic solution. The reason for this inaccuracy in the computed L_∞ *is* as follows. For problem 1, $\omega_o = 0.2$, the analytic k_∞ value is $k_\infty \approx 0.99937$. However, Eq. (12) becomes singular as $\theta_v \rightarrow 0$ $(\mu \rightarrow -1)$ when $k_\infty = 1$. For the nearly singular case at hand, both model II's eigenmatrix routine and the integral equation routines arc having a difficult time determining accurate values for k_∞ and L_∞. This is most noticeable in the $k_\infty = 1.0006$ value determined by model II; the theoretical upper limit for k_∞ *is* exactly one. Even slight errors in k_∞ cause large differences in L_∞ when k_∞ *is* near one. Author G.W.K. was able to obtain a satisfactory numerical solution of

Eq. (12) for this case only after resorting to quadruple-precision arithmetic. The $k_\infty \approx 0.87$ value seen in problem 2, $\omega_o = 0.2$, is far enough from one that no numerical difficulties arise. Note that the computation of k_∞ and L_∞ *is* a separate problem from the computation of the radiances and irradiances as discussed above. The inaccuracies in k_∞ and L_∞ just discussed in no way imply inaccuracies in the solution of Eq. (1).

V. Conclusions

Problems 1-3 of Sec. III cover the extreme range of oceanic inherent optical properties: ω_o from 0.2 to 0.9, phase functions for pure Rayleigh and pure particulate scattering, and strong vertical stratification. In computations of E_d and E_{ou}, the numerical models of Sec. II usually gave results within a few percent of each other throughout the euphotic zone. The spread in L_u values was as large as 12% in highly scattering waters, and much larger in highly absorbing waters at the bottom of the euphotic zone.

The statistical fluctuations of the Monte Carlo results from the true values of the predicted quantities are normally distributed. We therefore expect that more than 95% of the Monte Carlo simulations will be within two standard deviations (2σ) of the correct value. The data of Tab. V give us a feeling for the size of this 2cr-spread of values. Table VIII shows the 2σ-spread (expressed as a percentage of the mean) for E_d, E_{ou} and L_u in near-surface waters (based on τ = 1 for problems 1 and 2, and on z = 5 m for problem 3). Column 2 of the table shows typical errors in these radiometric quantities when measured by commercial instruments now in wide use. The third column of the table shows the accuracy desired in measurements to be used for ground-truth validation of the SeaWiFS ocean color satellite[55] (to be launched in 1994). Obtaining such accuracies in E_d and L_u measurements requires very careful instrument calibration,

We scc in Tab. VIII that the present numerical models easily compute E_d with greater accuracy than can be obtained with current instruments. Numerical estimates of E_{ou}, have about the same accuracy as measured values, The computed values of L_u arc less accurate than can be measured, or than arc needed for remote sensing studies requiring absolute radiometric values of L_u. Thus the Monte Carlo models should trace more photon histories, if very accurate L_u values are required. The standard deviation of the Monte Carlo fluctuations is proportional to $n^{-1/2}$, where n is the number of photons traced. Therefore the 20-spread seen in Tab. VIII can be cut in half by tracing four times as many photons, which is computationally practicable. Another possibility is to usc the backward Monte Carlo method, as described in Gordon[56].

Monte Carlo calculations using statistical estimation techniques can also yield continuum radiances, rather than quad-averaged values. Thus if one is interested in results for a few detectors located at precise angles, this technique can give highly accurate radiance values with only a very few photons being traced[57-59].

Values predicted by the Monte Carlo models generally fall on both sides of the values predicted by models 11 and DO, which do not have statistical fluctuations. Thus models 11 and DO have an advantage in the computation of upwelling quantities or in computations at great depths, which require tracing very large numbers of photons in the Monte Carlo codes.

The systematic differences in the atmospheric models used to simulate problem 4 lead to a 2cr-spread of order 20% in the computed radiometric quantities. Thus in order to compute acceptably accurate *absolute* radiometric values, more careful attention must be paid to how the incident radiance on the water surface is obtained. However, as noted before, systematic offsets in the absolute radiometric variables do not affect the values of apparent optical properties obtained from the radiometric variables. The present simple atmospheric models therefore all appear to be satisfactory for the computation of apparent optical properties,

Based on the problem solutions presented above, and on such comparisons between models and oceanographic measurements as have been ma-de (not discussed here), we conclude that each of the numerical models discussed here incorporates correct mathematical representations of the relevant radiative processes (absorption, elastic and inelastic scattering) and of the effects of the air-water boundary, Moreover, the models provide accurate numerical solutions of the associated equations. Each of these models is adequate for most of the needs of optical oceanography and limnology.

Appendix. Inelastic source function for model MC1.

As noted in Sec. II, model MC1 incorporates Raman scattering (and other inelastic processes, such as fluorescence) in an azimuthally averaged form suitable for the computation of inelastic scattering effects on irradiances. The corresponding mathematical form of the source function, which is used in the $-averaged version of Eq. (1), is developed as follows. This formulation is based on Chandrasekhar's[60] "n-approximation" solution of the radiative transfer equation,

The source function for inelastic processes is given by

$$S_{in}(z,\theta,\lambda) = \frac{1}{4\pi}\sum_{l=0}^{N} \int b_{in}^{(l)}(z,\lambda_{ex}\to\lambda)\, P_l(\cos\theta)\, E_l(z,\lambda_{ex})\, d\lambda_{ex} \,,$$

with

$$E_l(z,\lambda_{ex}) = 2\pi \int_0^{\pi} P_l(\cos\theta')\, L^{(0)}(z,\theta',\lambda_{ex}) \sin\theta'\, d\theta' \,,$$

and

$$\beta_{in}(z,\psi,\lambda_{ex}\to\lambda) = \frac{1}{4\pi}\sum_{l=0}^{N} b_{in}^{(l)}(z,\lambda_{ex}\to\lambda)\, P_l(\cos\psi) \,. \qquad \text{(A1)}$$

In these equations, P_l is the Legendre polynomial of order 1, N = O for isotropically emitted fluorescence, and N = 2 for Raman scattering. The total inelastic scattering coefficient $b_{in}^{(0)}$ is

$$b_{in}^{(0)}(z,\lambda_{ex}\to\lambda) \equiv b_{in}(z,\lambda_{ex}\to\lambda) = \int_{\Xi} \beta_{in}(z;\theta',\phi'\to\theta,\phi\,;\lambda_{ex}\to\lambda)\, d\Omega'$$

$$= 2\pi\int_0^{\pi} \beta_{in}(z,\psi,\lambda_{ex}\to\lambda) \sin\psi\, d\psi \,.$$

E_l for 1 = O is just the *scalar* irradiance at λ_{ex}, while E_l for l = 1 is the *net* irradiance $E_d - E_u$ at λ_{ex}. The inelastic component of the irradiance at λ depends only on the *irradiances* at the excitation wavelength(s) and on the $b_{in}^{(l)}$ coefficients for the particular process.

For Raman scattering, $\beta_{in} \equiv \beta_{Ram}$, and the angular distribution of β_{Ram} is given by

$$\beta_{Ram}(z,\psi,\lambda_{ex}\to\lambda) = \tilde{\beta}_{Ram}(\psi)\; b_{Ram}(z,\lambda_{ex}\to\lambda)\,, \tag{A.2}$$

where $\tilde{\beta}_{Ram}(\psi)$ is given by Eq. (9). Substituting Eq.(9) into Eq. (A.2) and rewriting in terms of the Legendre polynomials and the quantity $y \equiv (1-\rho)/(1+3p)$ gives

$$\beta_{Ram} = \frac{3}{16\pi}\left(\frac{1+3\rho}{1+2\rho}\right)\left[1 + \frac{1}{3}\gamma + \frac{2}{3}\gamma P_2(\cos\psi)\right] b_{Ram}(z,\lambda_{ex}\to\lambda)\,. \tag{A.3}$$

Comparing Eqs. (A. 1) and (A.3) reveals that

$$b^{(0)}_{Ram}(z,\lambda_{ex}\to\lambda) = b_{Ram}(z,\lambda_{ex}\to\lambda)\,,$$

$$b^{(2)}_{Ram} = \frac{1}{2}\left(\frac{11-\rho}{1+2\rho}\right) b_{Ram}(z,\lambda_{ex}\to\lambda)\;,$$

and that all of the other $b_{Ram}^{(l)}$ arc zero. Finally, the \$-averaged source function for Raman scattering is given by

$$S_{Ram}(z,\theta,\lambda) = \frac{1}{4\pi}\int b_{Ram}(z,\lambda_{ex}\to\lambda)\, E_o(z,\lambda_{ex})\left[1 + \frac{1}{2}\left(\frac{1-\rho}{1+2\rho}\right)\frac{E_2(z,\lambda_{ex})}{E_o(z,\lambda_{ex})} P_2(\cos\theta)\right] d\lambda_{ex}\,.$$

In general, at the emission wavelength λ, the source function resulting from a narrow band of excitation wavelengths $\Delta\lambda_{ex}$ is

$$S_{in}(z,\theta,\lambda) = \frac{1}{4\pi} b_{in}(z,\lambda_{ex}\to\lambda)\,\Delta\lambda_{ex}\, E_o(z,\lambda_{ex}) \sum_{l=0}^{N} \frac{b^{(l)}_{in}(z,\lambda_{ex}\to\lambda)\;\; E_l(z,\lambda_{ex})}{b_{in}(z,\lambda_{ex}\to\lambda)\;\; E_o(z,\lambda_{ex})}\, \mathit{P,(coSe)}\,. \tag{A.4}$$

To simulate the irradiances at λ, the basic Monte Carlo code for elastic scattering only is run at λ_{ex} to determine $E_l(z,\lambda_{ex})$. Then Eq. (A.4) is used to inject inelastically scattered photons into the medium with the proper distribution in z and θ. One way to do this is to choose z from the probability density $p(z)$ given by -

$$p(z) = \frac{E_o(z,\lambda_{ex})}{\int_o^{\infty} E_o(z,\lambda_{ex})\, dz} .$$

Thus, given a random number ρ_j from the sequence . ..$\rho_j, \rho_{j+1}, \rho_{j+2},\ldots,$ z is found from

$$\rho_j = \int_0^{z} p(z')\, dz' .$$

Given z, then θ is chosen from the conditional density $p(\theta\,|z)$ given by

$$p(\theta\,|z) = \frac{1}{4\pi} \sum_{l=0}^{N} \frac{b_{in}^{(l)}(z,\lambda_{ex} \to \lambda)\; E_l(z,\lambda_{ex})}{b_{in}(z,\lambda_{ex} \to \lambda)\; E_o(z,\lambda_{ex})} P_l(\cos\theta) ,$$

so that

$$\rho_{j+1} = \int_0^{\theta} p(\theta'\,|z)\, d\theta'$$

Finally, the rest of the source function must be incorporated into a photon weight

$$W = b_{in}(z,\lambda_{ex} \to \lambda)\, \Delta\lambda_{ex} \int_0 E_o(z,\lambda_{ex})\, dz ,$$

so that $S_{in}(z,\theta,\lambda) = Wp(z)p(\theta\,|z)$ as required. Once a photon is emitted at λ, it is followed in a manner similar to that which would be used in the absence of inelastic scattering, with the exception that inelastic scattering from λ to longer wavelengths is included by increasing the absorption coefficient $a(z,\lambda)$ by the appropriate inelastic scattering coefficient $b_{in}(z,\lambda \to \lambda')$ with $\lambda < \lambda'$ (recall, however, the discussion of this point in the definition of problem 7). In the code, $E_o(z,\lambda_{ex})$ *is* normalized to unit irradiance at λ_{ex} entering the top of the atmosphere normal to the solar beam, so the computed irradiances at λ (as seen in Tab. VI) are for unit irradiance at λ_{ex} entering the top of the atmosphere. This simulation technique was in part developed in this manner so that it could be used with *experimental* measurements of E_o to predict the inelastically scattered irradiances for a given process, e.g. Raman scattering. Such measurements can be obtained using instrumentation developed by Voss[61,62].

Acknowledgements

Author C.D.M. began this study with support from the Science Officer Research Program while he was at the' Office of Naval Research; subsequent work was performed while he was a National Research Council Research Associate at the Jet Propulsion Laboratory.

H.R.G. acknowledges support for this work from the Oceanic Optics Program of the Office of Naval Research under grant number NOOO 14-89-J-1 985.

G.W.K. was supported in part by the Oceanic Optics Program of the Office of Naval Research under grant number N0001 4-89-J-1467.

A.M. acknowledges the helpful technical assistance of B. Gentili in programming and running the Monte Carlo code. Hc is grateful for support from CHRS under contract UA353, and from ESA under grant ESTEC/3 15884,

P, R. performed this work while supported by NASA grants NAGW-465 and NAS5-30779, and by ONR grant N0001 4-89-J-1091.

R.H.S. acknowledges the stimulation, support and constructive criticism of Alan Weidemann and Rudolph Hollman of the Naval Research Laboratory, Stennis Space Center, MS. Grants of time on the Cray Y-MP were given by the North Carolina Supercomputing Center and the Primary Oceanographic Prediction System, U.S. Naval Oceanographic Office. He is grateful for continuing support from the Oceanic Optics Program, Office of Naval Research, under grant number N0001 4-89-J-3137.

References

1. F. Kneizys, E. Shettle, L. Abreu, J. Chetwynd, G. Anderson, W. Gallery, J. Selby and S, Clough, "Users guide to LOWTRAN-7," Air Force Geophysics Lab, rept. AFGL-TR-88-01 77, Hanscom AFB, MA, 137 pp.

2. C. Mobley, "A numerical model for the computation of radiance distributions in natural waters with wind-roughened surfaces," Limnol. Oceanogr. 34(8), 1473-1483 (1989).

3. C. Moblcy and R, Preisendorfer, "A numerical model for the computation of radiance distributions in natural waters with wind-roughened surfaces," NOAA Tech, Memo. ERL PMEL-75 (NTIS PB88-192703), Pac. Mar. Environ. Lab, Seattle, WA, 195 pp (1988).

4. R. Preisendorfer and C. Mobley, "Albedos and glitter patterns of a wind-roughened sca surface," J. Phys. Oceanogr. 16(7), 1293-1316 (1986).

5. A. Harrison and C. Coombes, "Angular distribution of clear sky short wavelength radiance," "Solar Energy 40, 57-69 (1988).

6. R. Preisendorfer, "Eigenmatrix representations of radiance distributions in layered natural waters with wind-roughened surfaces," NOAA Tech. Memo. ERL-PMEL-76 (NTIS PB88-188701), Pac. Mar, Environ. Lab., Seattle, WA 93 pp (1988).

7. C. Mobley, "A numerical model for the computation of radiance distributions in natural waters with wind-roughened surfaces, part 11: users' guide and code listing," NOAA Tech. Memo. ERL-PMEL-81 (NTIS PB88-246871), Pac. Mar. Environ. Lab., Seattle, WA, 170 pp (1988).

8. Z. Jin and K. Stamnes, "Radiative transfer in nonuniformly refracting layered media such as the atmosphere-ocean system, " submitted to Appl. Opt,

9. K. Stamnes and R.A. Swanson, "A new look at the discrete ordinate method for radiative transfer calculations in anisotropically scattering atmospheres," J. Atmos. Sci. 38(2), 387-399 (1981).

10. K. Stamnes and H. Dale, "A new look at the discrete ordinate method for radiative transfer calculations in anisotropically scattering atmospheres. 11: Intensity computations," J. Atmos. Sci. 38(1 2), 2696-2706 (198 1).

11. K. Stamnes, S.C. Tsay, W. Wiscombe, and K. Jayaweera, "Numerically stable algorithm for discrete-ordinate-method radiative transfer in multiple scattering and emitting layered media," Appl. Opt, *27, 2502-2509 (1988).*

12. H. Gordon, O. Brown and M, Jacobs, "Computed relationships between the inherent and apparent optical properties of a flat homogeneous ocean," Appl. Opt. 14, 417-427 (1975)

13. H. Gordon, "A bio-optical model describing the distribution of irradiance at the sea surface resulting from a point source embedded in the ocean," Appl. Opt. 26, 4133-4148 (1987).

14. H. Gordon, "Can the Lambert-Beer law be applied to the diffuse attenuation coefficient of ocean water?" Limnol. Oceanogr. 34, 1389-1409 (1989),

15, H. Gordon, "Dependence of the diffuse reflectance of natural waters on the sun angle," Limnol. Oceanogr. 34, 1484-1489 (1989),

16. H. Gordon, "Diffuse reflectance of the ocean: influence of nonuniform phytoplankton pigment profile," Appl. Opt. 31, 2116-2129 (1992).

17. Y. Ge, H. Gordon and K. Voss, "Effect of Raman scattering on Fraunhofer lines in the ocean," Appl. Opt., in press,

18. C. Cox and W. Munk, "Statistics of the sea surface derived from sun glitter," J. Mar. Res. 13, 198-227 (1954).

19. L. Elterman, "UV, visible, and IR attenuation for altitudes to 50 km," Report AFCRL-68-0153, Air Force Cambridge Res. Lab., Bedford MA, 49 pp (1968).

20, G. Mie, "Beiträge zur optik trüber medien, speziell kolloidalen metal] -losengen," Ann. Phys. 2S, 377-445 (1908).

21, D. Deirmendjian, "Scattering and polarization properties of polydisperse suspensions with partial absorption," in *Electromagnetic Scattering,* edited by M. Kerker, Pergamon, New York, 171-189 (1963).

22. G. Kattawar and X. Xu, "Filling-in of Fraunhofer lines in the ocean by Raman scattering," Appl. Opt. **31**, 1055-1065 (1 992).

23. G. Kattawar and C. Adams, "Stokes vector calculations of the submarine light field in an atmosphere-ocean with scattering according to a Rayleigh phase matrix: effect of interface refractive index on radiance and polarization, " Limnol. Oceanogr. 34, 1453-1472 (1989).

24, G. Kattawar and C, Adams, "Errors in radiance calculations induced by using scalar rather than Stokes vector theory in a realistic atmosphere-ocean system," *Ocean Optics X,* R, Spinrad, cd., Proc. SPIE 1302, 2-12 (1990).

25. C. Adams and G. Kattawar, "Effect of volume scattering function on the errors induced when polarization is neglected in radiance calculations in an atmosphere-ocean system," Appl. .,Opt., in press,

26. G. Kattawar and C. Adams, "Errors induced when polarization is neglected in radiance calculations for an atmosphere-ocean system ," Ocean *Optics XI, G.* Gilbert, cd., Proc. SPIE, in press.

27. G. Plass and G. Kattawar, "Radiative transfer in an atmosphere-ocean system," Appl. Opt. 8, 455-466 (1 969).

28. G. Plass and G. Kattawar, "Monte-Carlo calculations of radiative transfer in the earth's atmosphere ocean system: I, flux in the atmosphere and ocean," J. Phys. Oceanogr. 2, 139-145 (1972).

29. H, Gordon and O. Brown, "Irradiance reflectivity of a flat ocean as a function of its optical properties," Appl. Opt. **12**, 1549-1551 (1973).

30. G. Plass, G. Kattawar and J. Guinn, Jr., "Radiative transfer in the earth's atmosphere and ocean: influence of ocean waves," Appl. Opt. 14, 1924-1936 (1975).

31. A. Morel and B. Gentili, "Diffuse reflectance of oceanic waters: its dependence on sun angle as influenced by the molecular scattering contribution," Appl. Opt. 30, 4427-4438 (1991).

32. A. Morel and B. Gentili, "Diffuse reflectance of oceanic waters (2): bi-directional aspects," Appl. Opt., in press,

33. D. Tanré, M. Herman, R. Deschamps and A. deLeffe, "Atmospheric modeling for space measurements of ground reflectances including bi-directional properties," Appl. Opt. **18**, 3587-3594 (1979).

34. K. Baker and R, Frouin, "Relation between photosynthetically available radiation and total insolation at the ocean surface under clear skies," Limnol. Oceanogr. 32, 1370-1377 (1987).

35. J. Kirk, "Monte Carlo procedure for simulating the penetration of light into natural waters," Div. Plant Industry Tech. Paper 36, CSIRO, Canberra, Australia, 16 pp (1981).

36. H. Gordon and D. Castano, "Coastal zone color scanner atmospheric correction algorithm: multiple scattering effects," Appl. opt. 26, 2111 (1 987).

37. W. Blattner, H. Horak, D. Collins, and M. Wells, "Monte Carlo studies of the sky radiation at twilight," Appl Opt, 13, 534 (1974).

38. R. Stavn and A. Weidemann, "Optical modeling of clear ocean light fields: Raman scattering effects," Appl. Opt. 27, 4002-4011 (1988).

39. R. Stavn and A. Weidemann, "Raman scattering in ocean optics: quantitative assessment of internal radiant emission," Appl. Opt. 31, 1294-1303 (1992).

40. D. Brine and M. Iqbal, "Diffuse and global solar spectral irradiance under cloudless skies," Solar Energy 30, 447-453 (1983).

41. T, Petzold, "Volume scattering functions for selected ocean waters," S10 Ref. 72-78, Scripps Inst. Oceanogr., La Jolla, CA, 79 pp (1972).

42. A. Morel, "Optical properties of pure water and pure sea water," In *Optical Aspects of Oceanography,* Jerlov and Nielsen, eds., Academic Press, pp 1-24 (1974),

43, R, Smith and K. Baker, “Optical properties of the clearest natural waters (200-800 rim),” Appl. Opt. 20, 177-184 (1981).

44. L. Pricur and S. Sathyendranath, “An optical classification of coastal and oceanic water based on the specific spectral absorption curves of phytoplankton pigments, dissolved organic matter, and other particulate materials," Limnol. Oceanogr. 26(4), 671-689 (1981).

45. H. Gordon and A, Morel, “Remote assessment of ocean color for interpretation of satellite visible imagers, a review,” Lecture notes on coastal and estuarine studies 4, Springer Verlag, 114 pp (1 983).

46. M. Lewis, J, Cullen and T. Platt, "Phytoplankton and thermal structure in the upper ocean: consequences of nonuniformity in chlorophyll profile,” J. Geophys. Res. 88 (C4), 2565-2570 (1983),

47. T. Platt and S. Sathyendranath, “Oceanic primary production: estimation by remote sensing at local and regional scales,” Science 241, 1613-1620 (1988).

48. S. Porto, “Angular dependence and depolarization ratio of the Raman effect,” J. Opt, Sot. Am. 56, 1585-1589 (1966).

49, R, Prciscndorfcr, *Hydrologic Optics, volume V, Properties,* U.S. Dept. of Commerce, Pacific Marine Environmental Lab., Seattle, Wa., 296 pp (1976).

50. G. Kattawar and G. Plass, “Asymptotic radiance and polarization in optically thick media: ocean and clouds,” Appl. Opt, 15(12), 3166-3178 (1976).

51. R. Stavn, R. Schiebe and C. Gallegos, “Optical controls on the radiant energy dynamics of the air/water interface: the average cosine and the absorption coefficient," Ocean Optics VII, M, Blizard, Editor, Proc. SPIE 489, 62-67 (1984).

52. G. Plass, T. Humphreys and G. Kattawar, “Occ~n-atmosphere interface: its influence on radiation,” Appl. Opt, 20, 917-931 (1981).

53. H. van dc Hulst, *Multiple Light Scattering: Tables, Formulas, and Applications,* vol. 1, Academic Press, Ncw York, 299 pp (1980).

54. "L, Pricur and A. Morel, "Etude theorique du regime asymptotique: relations entre caracteristiques optiques et coefficient d'extinction relatif a la penetration de la lumiere du jour," Cab. Oceanogr. 23, 35 (1971).

55, J. Mueller and R. Austin, , "Ocean optics protocols for SeaWiFS validation," SeaWiFS project technical report vol. 5, series editors S. B, Hooker and E. R. Firestone, NASA tech, memo. 104566, 43 pp. (July 1992).

56. H. Gordon, "Ship perturbation of irradiance measurements at sea. 1: Monte Carlo simulations," Appl. Opt. 24(23), 4172-4182 (1985).

57. C. Adams and G. Kattawar, "Radiative transfer in spherical shell atmospheres: Rayleigh scattering," Icarus, 35, 139-151 (1978).

58. G. Kattawar and C. Adams, "Radiative transfer in spherical shell atmospheres. II. Asymmetric phase functions," Icarus. 35, 436-449 (1978).

59. G. Kattawar, "Radiative transfer in spherical shell atmospheres. III. Application to Venus," Icarus. 40, 60-66 (1979).

60, S. Chandrasekhar, *Radiative Transfer,* Dover, New York, 393 pp. (1960).

61. K. Voss, "Electro-optic camera system for measurement of the underwater radiance distribution," Opt, Eng. 28, 241-247 (1989)

62. K. Voss, "Use of the radiance distribution to measure the optical absorption coefficient in the ocean," Limnol. Oceanogr. 34, 1614-1622 (1989).

Table 1. Significant symbols, units and definitions.

Symbol	Units	Definition
λ	nm	the wavelength of light
ψ	deg	the scattering angle; $O \le \psi \le 180°$
θ	deg	the polar angle of photon travel, measured from the nadir, $0 \le \theta \le 180°$
ϕ	deg	the azimuthal angle of photon travel, measured counterclockwise (looking downward) from the downwind direction, $O \le \phi$ c $360°$
μ	–	$\mu \equiv \cos\theta$; alternate way to specify the polar angle, $-1 \le \mu \le 1$
θ_v	deg	the polar viewing angle: $\theta_v = 180° - \theta$
ϕ_v	deg	the azimuthal viewing angle: $\phi_v = 180° + \phi$
Ω	sr	solid angle; a differential element is $d\Omega = \sin\theta\, d\theta\, d\phi = d\mu\, d\phi$
Ξ_d	–	the set of all downward directions; $\int_{\Xi_d} d\Omega = 2\pi$ sr
Ξ_u	–	the set of all upward directions; $\int_{\Xi_u} d\Omega = 2\pi$ sr
z	m	geometric depth, measured positive downward
τ		optical depth, measured positive downward: $\tau \equiv \int_0^z c(z)\,dz$
σ	–	the standard deviation of the surface wave slope
a_w	m^{-1}	the absorption coefficient for pure sca water
a_p	m^{-1}	the absorption coefficient for suspended particles
a	m^{-1}	the total absorption coefficient: $a \equiv a_w + a_p$
b_w	m^{-1}	the scattering coefficient for pure sca water
b_p	m^{-1}	the scattering coefficient for suspended particles
b	m^{-1}	the total scattering coefficient: $b \equiv b_w + b_p$
c	m^{-1}	the total attenuation coefficient: $c \equiv a + b$

β	$m^{-1}\ sr^{-1}$	the volume scattering function
$\tilde{\beta}$	sr^{-1}	the scattering phase function, $\tilde{\beta} \equiv \beta/b$
0.)$_0$	–	the scattering-to-attenuation ratio, $\omega_o \equiv b/c$
L	W $m^{-2}\ sr^{-1}$ ri^m-’	the radiance distribution, $L = L(z,\theta,\phi)$ or $L(\tau,\mu,\phi)$
L_u	W $m^{-2}\ sr^{-1}$ rim-l	the nadir radiance, $L_u \equiv L_u(\tau) \equiv L(\tau,\theta{=}180,\phi{=}0)$
L_∞	W $m^{-2}\ sr^{-1}$ rim-l	the asymptotic radiance distribution
k_∞		the asymptotic diffuse attenuation coefficient
s	W m“^{2} $sr^{-1}\ nm^{-1}$	an internal source of radiance
$E_\perp$	W $m^{-2}\ nm^{-1}$	irradiance on a surface perpendicular to the sun’s rays
E_d	W m^{-2} rim-l	downwelling plane irradiance: $E_d(\tau) \equiv \int_{\Xi_d} L(\tau,\mu,\phi)\,|\mu|\,d\Omega$
E_u	W m^{-2} rim-l	upwelling plane irradiance: $E_u(\tau) = \int_{\Xi_u} L(\tau,\mu,\phi)\,|\mu|\,d\Omega$
E_{ou}	W m^{-2} rim-l	the upwelling scalar irradiance: $E_{ou}(\tau) \equiv \int_{\Xi_u} L(\tau,\mu,\phi)\,d\Omega$

Table Il. Phase function values used in defining the particulate phase function $\tilde{\beta}_p(\psi)$. The notation n±e means n×10$^{\pm e}$.

Scattering angle (deg)	Phase function (sr^{-1})	Scattering angle (deg)	Phase function (sr^{-1})
0,10000	1.76661+3	50.0	2.27533-2
0.12589	1.29564+3	55.0	1.69904-2
0.15849	9.50172+2	60.0	1.31254-2
0.19953	6.99092+2	65.0	1.04625-2
0.25119	5.13687+2	70.0	8.48826-3
0.31623	3.76373+2	75.0	6.97601-3
0.39811	2.76318+2	80.0	5.84232-3
0.50119	2.18839+2	85.0	4.95306-3
0.63096	1.44369+2	90.0	4.29232-3
0.79433	1.02241+2	95.0	3.78161-3
1.0000	7.16082+1	100.0	3.40405-3
1,2589	4.95803+1	105.0	3.11591-3
1.5849	3.39511+1	110.0	2.91222-3
1.9953	2.28129+1	115.0	2.79696-3
2.5119	1.51622+1	120.0	2.68568-3
3,1623	1.00154+1	125.0	2.57142-3

3.9811	6.57957	130.0	2.47603-3
5.0119	4.29530	135.0	2.37667-3
6.3096	2,80690	140.0	2.32898-3
7,9433	1.81927	145.0	2.31308-3
10.0	1.15257	150.0	2.36475-3
15.0	4.89344-1	155.0	2.50584-3
20,0	2.44424-1	160.0	2.66183-3
25.0	1,47151-1	165.0	2.83472-3
30.0	8.60848-2	170.0	3.03046-3
35.0	5.93075-2	175.0	3.09206-3
40.0	4.20985-2	180.0	3.15366-3
45.0	3.06722-2		

Table 111. Summary of the canonical problems.

Parameter	Problem 1 easy problem	2 base problem	3 stratified water	4 atmospheric effects	5 wind-blown surface	6 bottom effects	7 Raman scattering
albedo, ω_o	0.9, 0.2	0.9, 0.2	depth dependent	0.9	0.9	0.2	0.29 at 417 nm 0.15 at 486 nm
phase function	Rayleigh Eq. (3)	particle Tab. 11	depth dependent	particle Tab. II	particle Tab. II	particle Tab. II	Eq. (3) and Eq. (9)
air- water surface	flat	flat	flat	flat	capillary waves	flat	flat
diffuse sky radiance	o	0	0	various models	o	0	0
internal sources	0	0	0	0	0	0	various models
bottom boundary	infinitely deep	infinitely deep	infinitely deep	infinitely deep	infinitely deep	lambertian at $\tau = 5$	infinitely deep

Table.IV. Representative execution times, and numbers of simulated photons for models MC1-MC5.

Problem	Execution time (sCc)	Number of photons initiated	Number of photon collisons
Model 11 (Computer: Sun SPARCstation 2, no code optimization):			
1,6.). = 0.9	349 for τ = 10; 730 for τ = 20		
1,0. = 0.2	350 for τ = 10; 733 for τ = 20		
2, ω_o = 0.9	306 for τ = 10; 496 for τ = 20		
2, ω_o = 0.2	386 for τ = 10; 711 for τ = 20		
3	1180 for z = 60 m		
Model DO (Computer: Decstation 5000/240, no code optimization)			
1, ω_o = 0.9	5 for irradiances only, 2 layers		
1, ω_o = 0.2	5 for irradiances only, 2 layers		
2, ω_o = 0.9	9 for irradiances only, 2 layers; 435 for radiances, 2 layers		
2, ω_o = 0.2	9 for irradiances only, 2 layers		
3	171 for irradiances only, 25 layers		
Model MC1 (Computer: Decstation 5000)			
1,0. = 0.9	7200	1.25x o'	4.98×10^{7}
1, ω_o = 0.2	7200	6.63x 0^{6}	3.99×10^{7}
2, ω_o = 0.9	7200	9.66x1O'	7.18×10^{7}
2, ω_o = 0.2	7200	7. I7X1O'	3.77×10^{7}
3	7200	7.49x 106	8.74×10^{7}

Model MC2 (Computer: Vax 9000)			
1, ω_o = 0.9	5830	1. 0X10’	$9.47X10^7$
1, ω_o = 0.2	530	1. 0X10’	$7.54X10^7$
2, ω_o = 0.9	4630	$I.0X10^6$	$9.72x10^7$
2, ω_o = 0.2	410	$1.0X10^6$	$7.85x10^7$
Model MC3 (Computer: Hewlett Packard 9000/730)			
1, ω_o = 0.9	60000	10.9X1O’	$6.72x10^8$
1, ω_o = 0.2	74000	$55.7X10^6$	7.07X 108
2, ω_o = 0.9	45000	8.7x1O’	7.30X 108
2, ω_o = 0.2	84000	63.7x1O’	12.10X 108
3	56000	8.9x1O’	$9.02x10^8$
Model MC4 (Computer: Microvax 111)			
1, ω_o = 0.9	15100	5.0X 104	$1.66X10^7$
1, ω_o = 0.2	17700	$1.0X10^6$	1.44X 107
2, ω_o = 0.9	9680	8.0x 104	$1.24x10^7$
2, ω_o = 0.2	10000	$1.2X10^6$	$I.02X10^7$
3	24200	1.0×10^5	3.06×10^7
Model MC5 (Computer: Cray Y-MP, no vectorization)			
1, ω_o = 0.9	1981 for τ = 20	1.0×10^7	
1,0. = 0.2	416 for τ = 10	$I.0X10^7$	
2, ω_o = 0.9	2300 for τ = 20	$1.0X10^7$	
2, ω_o = 0.2	389 for τ = 10	$I,0X10^7$	

Table V. Average values of E_d, E_{ou} and L_u at selected depths for problems 1-6. N is the number of models included in the averages, The ratio of the sample standard deviation to the sample mean, $s/\bar{x}$, is also displayed for each average value. The average values are relative to an incident solar irradiance of $E_\perp$ = *1.0* W m^{-2} rim-l incident on the water surface, except for problem 4, for which $E_\perp$ *is* applied at the top of the atmosphere. The notation 3.66-1 means 3.66x 10-], etc.

optical	average value			corresponding $s/\bar{x}$		
depth	E_d	E_{ou}	L_u	E_d	E_{ou}	L_u
Problem 1, ω_o = 0.9 (N = 7)						
1	3.66-1	3.72-1	4.85-2	0.002	0.005	0.015
5	4.33-2	4.35-2	5.59-3	0.003	0.007	0.052
10	3.16-3	3.20-3	4.37-4	0.015	0.038	0.091
Problem 1, ω_o = 0.2 (N = 7)						
1	1.41-1	1.34-2	1.72-3	0.001	0.003	0.044
5	1.07-3	1.00-4	1.37-5	0.005	0.039	0.288
10	2.93-6	3.00-7	3.39-8 (N=4)	0.102	0.308	0.197
Problem 2, ω_o = 0.9 (N = 7)						
1“	4.13-1	9.31-2	6.99-3	0.001	0.021	0.063
5	1.87-1	4,63-2	3.26-3	0.005	0.017	0.055
10	6.85-2	1.65-2	1.21-3	0.010	0.014	0.109

Problem 2, $\omega_o = 0.2$ (N = 7)						
1	1.62-1	9.66-4	5.47-5	**0.000**	0.023	0.060
5	2.27-3	1.37-5	6.24-7 (N=6)	0.002	0.063	0.355
10	1.30-5	7.28-8	4.02-9 (N=5)	0.047	0.187	0.248
Problem 3 (N = 6)						
5 m	2.30-1	4.34-2	3.13-3	0.006	0.025	0.054
25 m	1.62-3	2.86-4	2.12-5	0.028	0.038	0.061
60 m	5.23-5	5.13-6	3.57-7	0.071	0.036	0.434
Problem 4 (N = 6)[a]						
1	3.23-1	7.13-2	5.63-3	0.076	0.091	0.111
5	1.49-1	3.57-2	2.77-3	0.072	0.076	0.141
10	5.56-2	1.31-2	9.60-4	0.070	0.073	0.107
Problem 5 (N = 4)						
1	1.14-1	3.55-2	2.09-3	0.012	0.020	0.031
5	4.33-2	1.22-2	7.63-4	0.009	0.028	0.036
10	1.48-2	3.65-3	2.49-4	0.007	0.020	0.025
Problem 6 (N = 3)						
1	1.62-1	9.81-4	6.84-5	0.000	0.010	0.020
5	2,28-3	2.28-3	3.60-4	0.003	0.002	0.010

a. $s/\bar{x}$ values determined by systematic offset; see discussion in the text,

Table VI. Raman scattering contributions to E_d and E_u at λ = 486 nm from an excitation wavelength of λ_{ex} = 417 nrn. Parameter values arc given in the specification of problem 7. Values in the body of the table have units of W m^{-2} nm^{-1} for an incident irradiance of $E_{\perp}$ = *1.0* *w* m^{-2} nm^{-1} at λ_{ex}.

depth	model			
(m)	MC1	MC2	MC3	MC5
E_d values:				
0	0.01875	0.01874	0.01739	0.01873
50	0.02489	0.02488	0,02470	0.02490
100	0.01136	0.01136	0.01123	0.01138
E_u values:				
o	0.03532	0.03512	0.03478	0.03523
50	0.01034	0.01042	0.01027	0.01039
100	0.00287	0.00296	0.00292	0.00296

Table VII. Computed values of k_∞.

Problem	Model				
	II	DO	MC1[a]	MC2	MC3
1, $\omega_o = 0.9$	**0.5248**	**0.5232**	**0.52**	**0.5232**	**0.5235**
1, $\omega_o = 0.2$	**1.0006**	**0.9994**	–	**0.9996**	**0.9952**
2, $\omega_o = 0.9$	0.1920	0.2068	0.189	0.1835	0.1879
2, $\omega_o = 0.2$	0.8737	0.8794	-	0.8590	0.8619

a. Values determined by visual inspection of plotted output,

Table VIII. Comparison of accuracies for computing and measuring radiometric variables.

Variable	2cr-spread of model values	current measurement capability	target accuracy for SeaWiFS[a]
E_d	1 %	3-5 %	2 %
E_{ou}	5%	3-5 %	
L_u	12 %	3-5 %	3 %

a. from Mueller and Austin[55]

FIGURE CAPTIONS

Fig. 1. Panel a shows inherent optical properties as a function of depth for problem 3. Coefficients *a, b,* and c have units of m“]; ω_o is dimensionless. Panel b shows the scattering phase function for pure sca water, $\tilde{\beta}_w$; for particles, $\tilde{\beta}_p$; and for problem 3 at depths of z = O, 17 m, and 60 m.

Fig. **2.** Panel a shows E_d, E_{ou}, and L_u as computed by the various models for problem 1, ω_o **= 0.9.** Panel b shows the same quantities as computed for the case of ω_o = 0.2. The dotted line represents the air-water surface. Results from models II and DO are plotted with solid lines; models MC1 -MC5 with dashed lines. Depth τ = O is in the water, just below the surface, and “in air” represents a point just above the surface.

Fig. **3** Model predictions for problem 2, the “base” case. Panel a is for ω_o = 0.9 and panel b is for ω_o = 0.2.

Fig. 4 Model predictions for problem 3, the stratified-water case.

Fig. 5 E_d near the surface for problem 4, the base case plus an atmosphere.

Fig. 6 Model predictions near the surface for problem 5, the capillary-wave case. The wind speed is *U* = 7.23 m S-l, and the zenith angle of the sun is θ_{sun} = 80°.

Fig. 7. Model predictions for problem 6, the finite-depth case. The bottom reflectance is 0.5.

Fig. 8 Radiance distribution in the plane of the sun for problem 2, ω_o = 0.9. Angles (θ_v,ϕ_v) arc viewing directions: θ_v = 180°- θ and ϕ_v = 180° + ϕ, where (θ,ϕ) arc the directions of photon travel. Solid lines arc $L(\tau,\theta_v,\phi_v)$ at selected depths within the water; the dotted line is the asymptotic distribution $L_\infty(\theta_v)$ normalized to the largest value of L at $\tau = 20$.

Fig. **9** Asymptotic radiance distributions $L_\infty(\theta_v)$ for problems 1 and 2, as computed by various models (solid lines). The dotted lines give the exact analytic solution[46] for the Rayleigh phase function of problem 1.

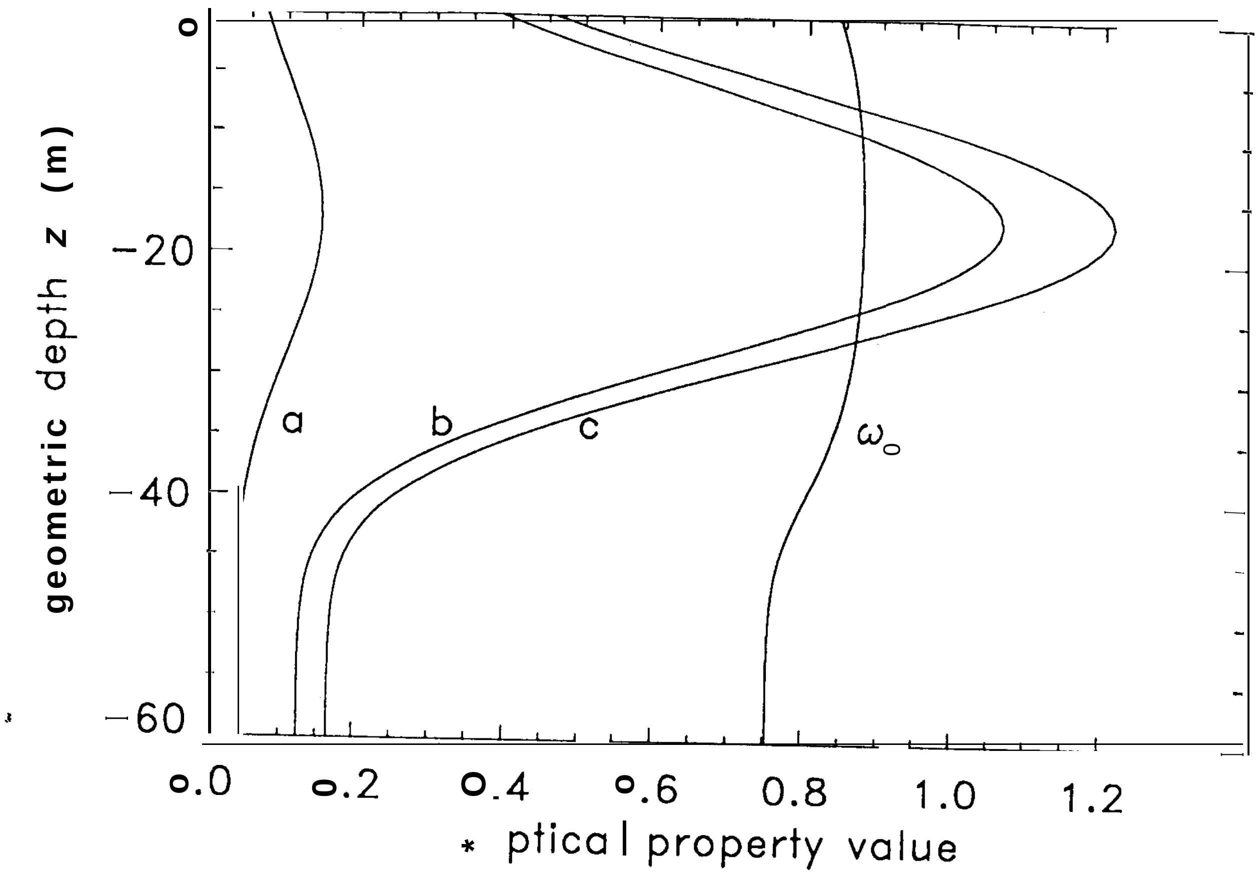
geometric depth z (m)
0
−20
−40
−60
o.0
o.2
O.4
o.6
0.8
1.0
1.2
* ptical property value
a
b
c
ω0

Fig (a)

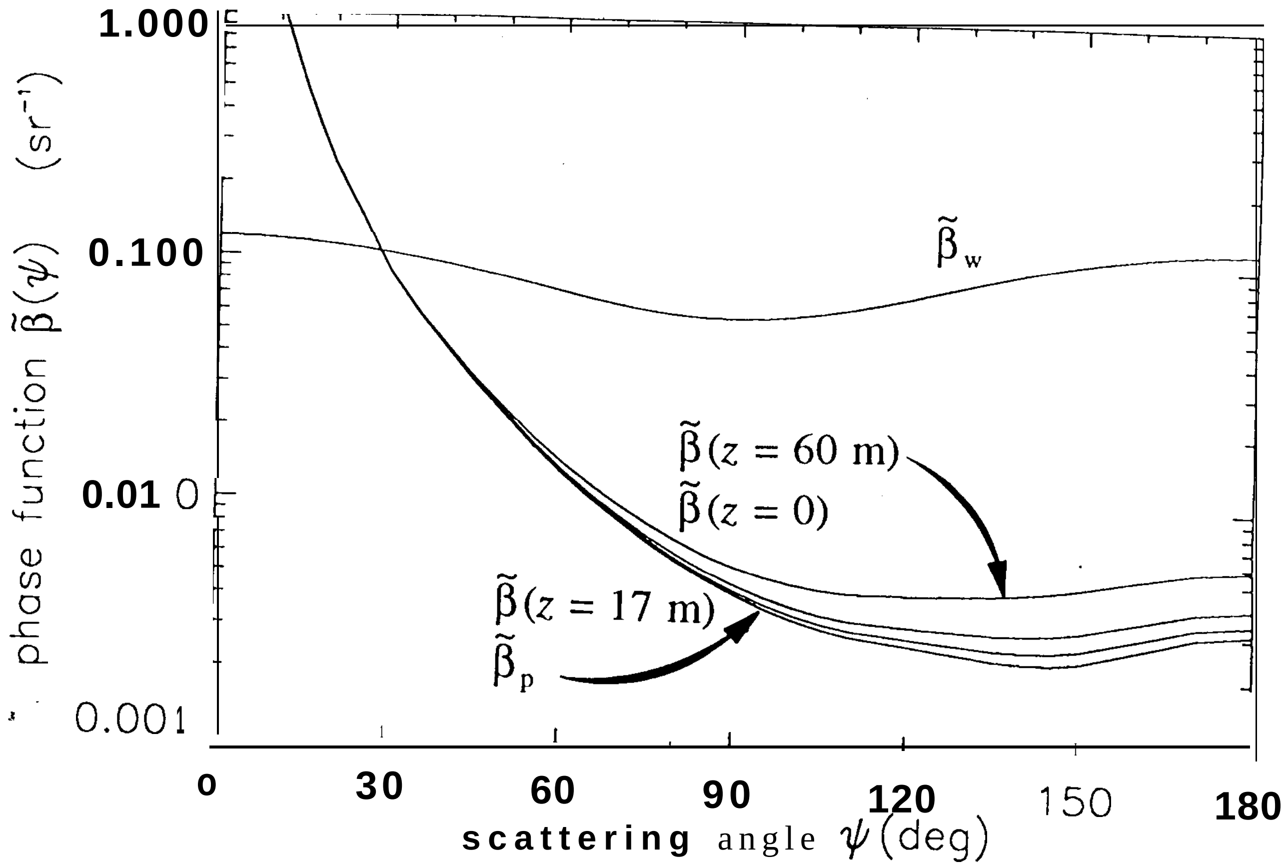

1.000
0.100
0.01 0
0.001
phase function $\tilde{\beta}(\psi)$ (sr^{-1})
$\tilde{\beta}_w$
$\tilde{\beta}(z = 60\ m)$
$\tilde{\beta}(z = 0)$
$\tilde{\beta}(z = 17\ m)$
$\tilde{\beta}_p$
0
30
60
90
120
150
180
scattering angle ψ (deg)

Fig 1(b)

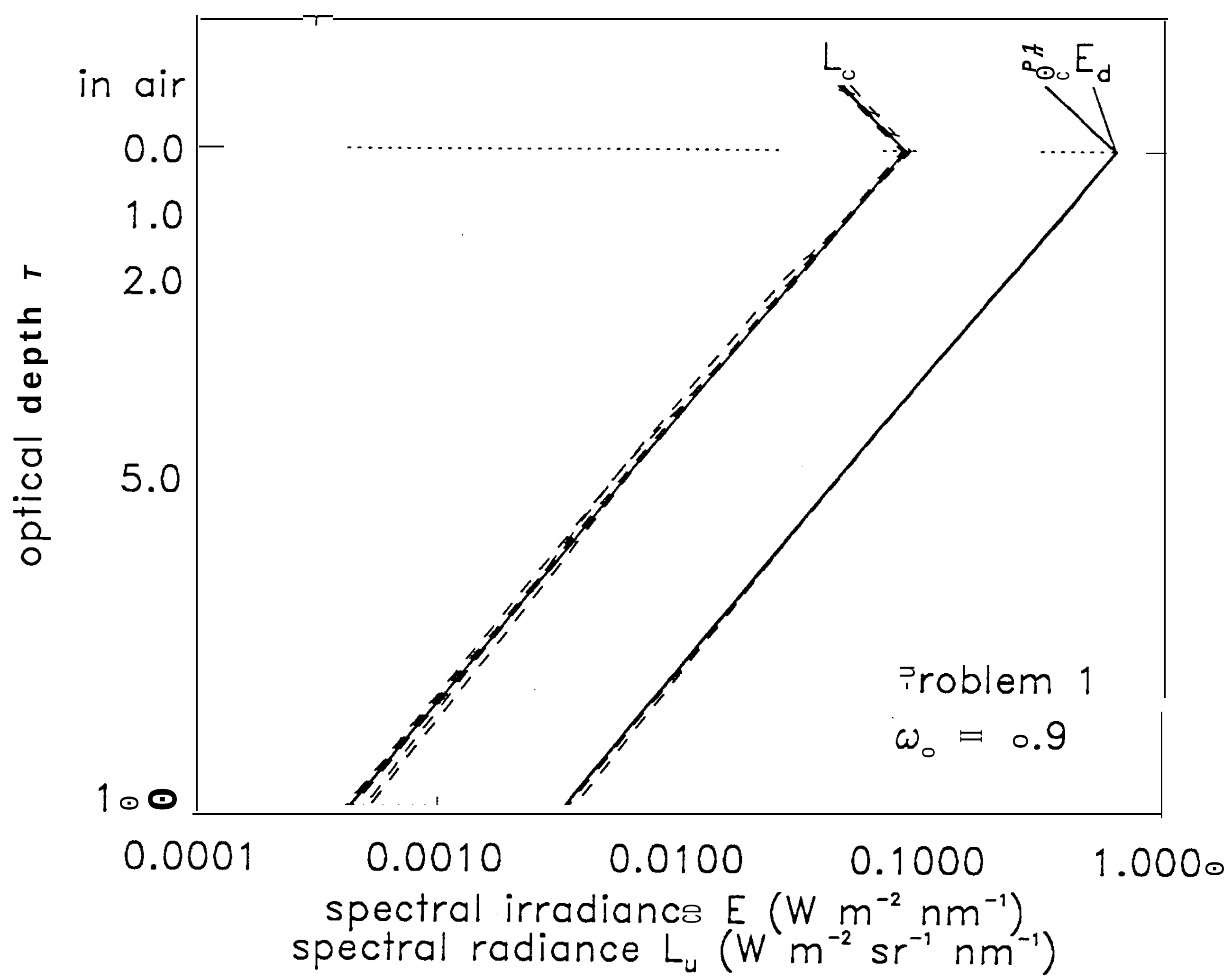

in air
0.0
1.0
2.0
5.0
10
optical depth τ
0.0001
0.0010
0.0100
0.1000
1.0000
spectral irradiance E (W m^-2 nm^-1)
spectral radiance L_u (W m^-2 sr^-1 nm^-1)
L_u
E_d
Problem 1
ω_o = 0.9

Fig. 2(a)

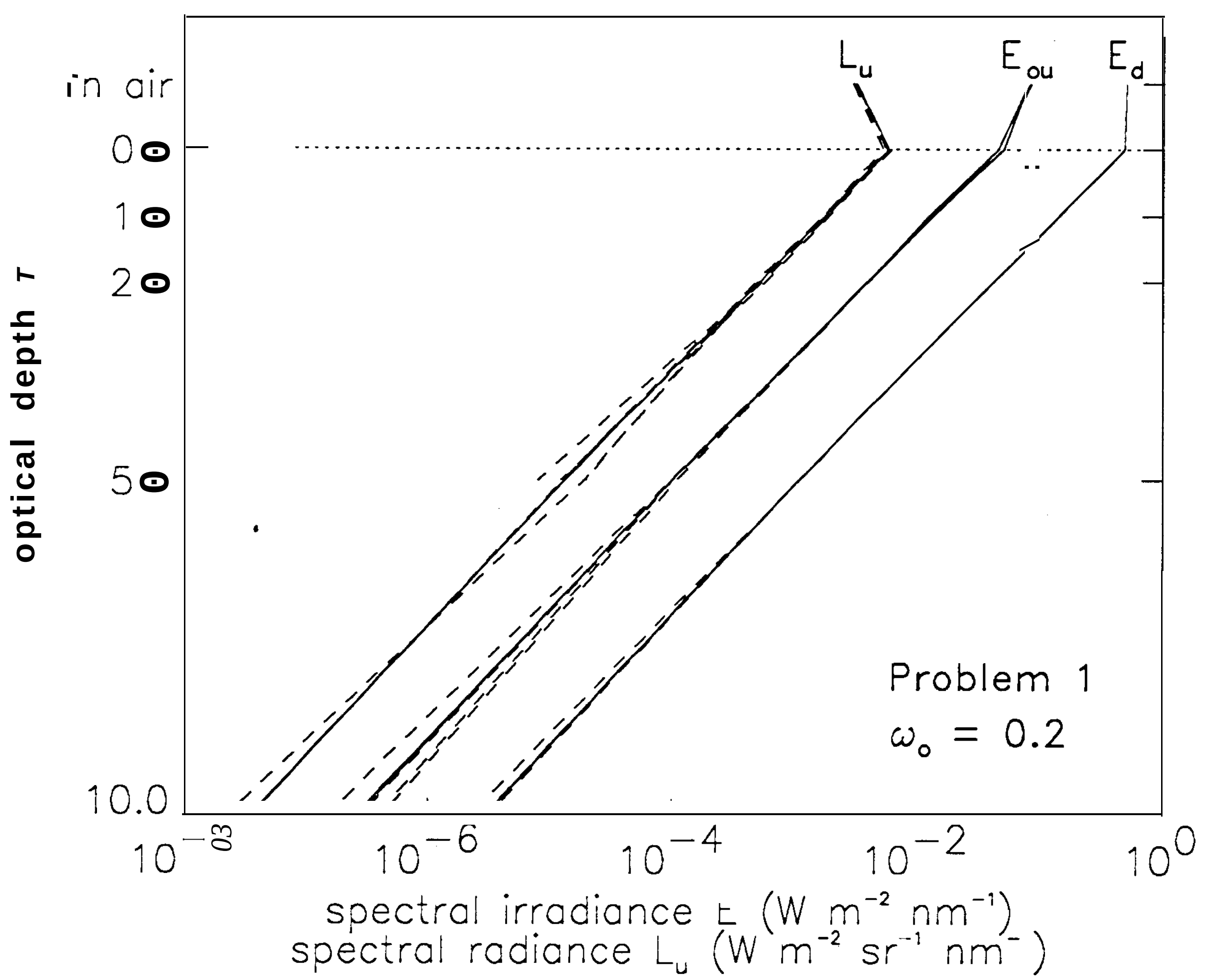
optical depth τ
in air
0.0
1.0
2.0
5.0
10.0
L_u
E_ou
E_d
Problem 1
ω_o = 0.2
10^-03
10^-6
10^-4
10^-2
10^0
spectral irradiance E (W m^-2 nm^-1)
spectral radiance L_u (W m^-2 sr^-1 nm^-)

Fig. 2(b)

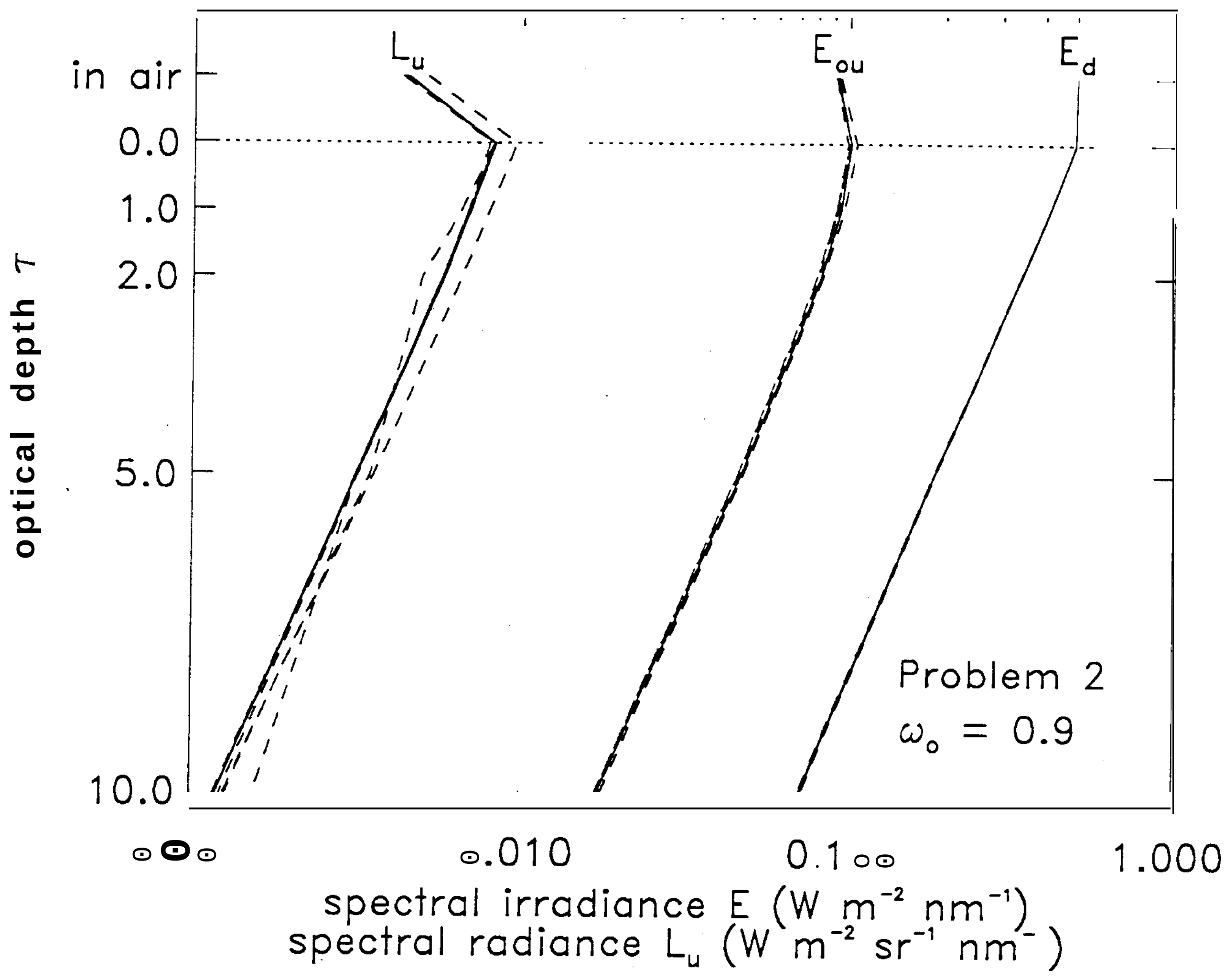

optical depth τ
in air
0.0
1.0
2.0
5.0
10.0
L_u
E_{ou}
E_d
Problem 2
$\omega_o = 0.9$
0.001
0.010
0.100
1.000
spectral irradiance E (W m^{-2} nm^{-1})
spectral radiance L_u (W m^{-2} sr^{-1} nm^{-})

Fig. 3(a)

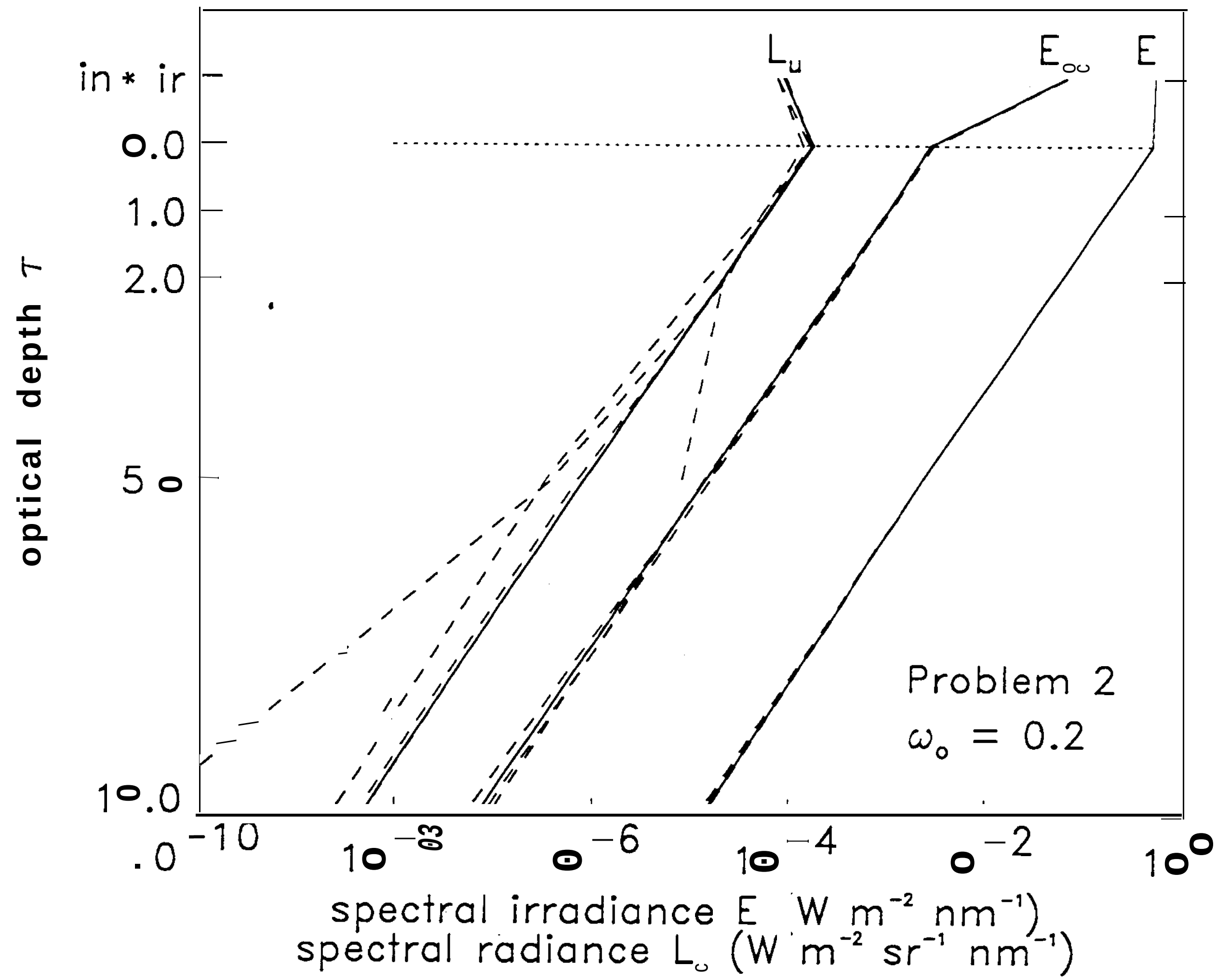

optical depth τ
in * ir
0.0
1.0
2.0
5 0
10.0
.0 −10
10 −03
0 −6
10 −4
0 −2
10 0
L_u
$E_{o\infty}$
E
Problem 2
$\omega_o = 0.2$
spectral irradiance E W m−2 nm−1)
spectral radiance L_o (W m−2 sr−1 nm−1)

Fig. 3(b)

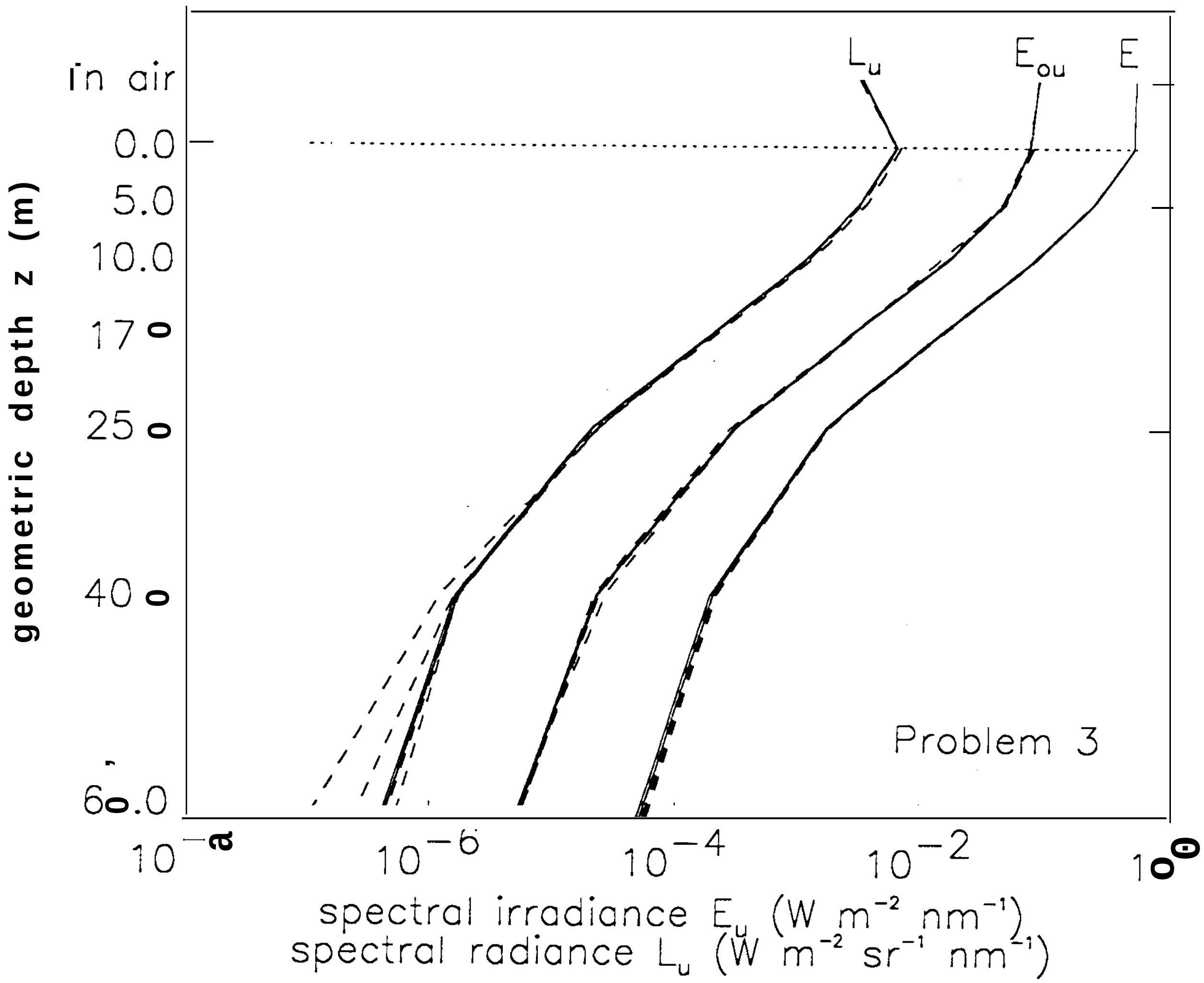

geometric depth z (m)
in air
0.0
5.0
10.0
17.0
25.0
40.0
60.0
L_u
E_{ou}
E
Problem 3
10^{-8}
10^{-6}
10^{-4}
10^{-2}
10^{0}
spectral irradiance E_u (W m^{-2} nm^{-1})
spectral radiance L_u (W m^{-2} sr^{-1} nm^{-1})

Fig. 4

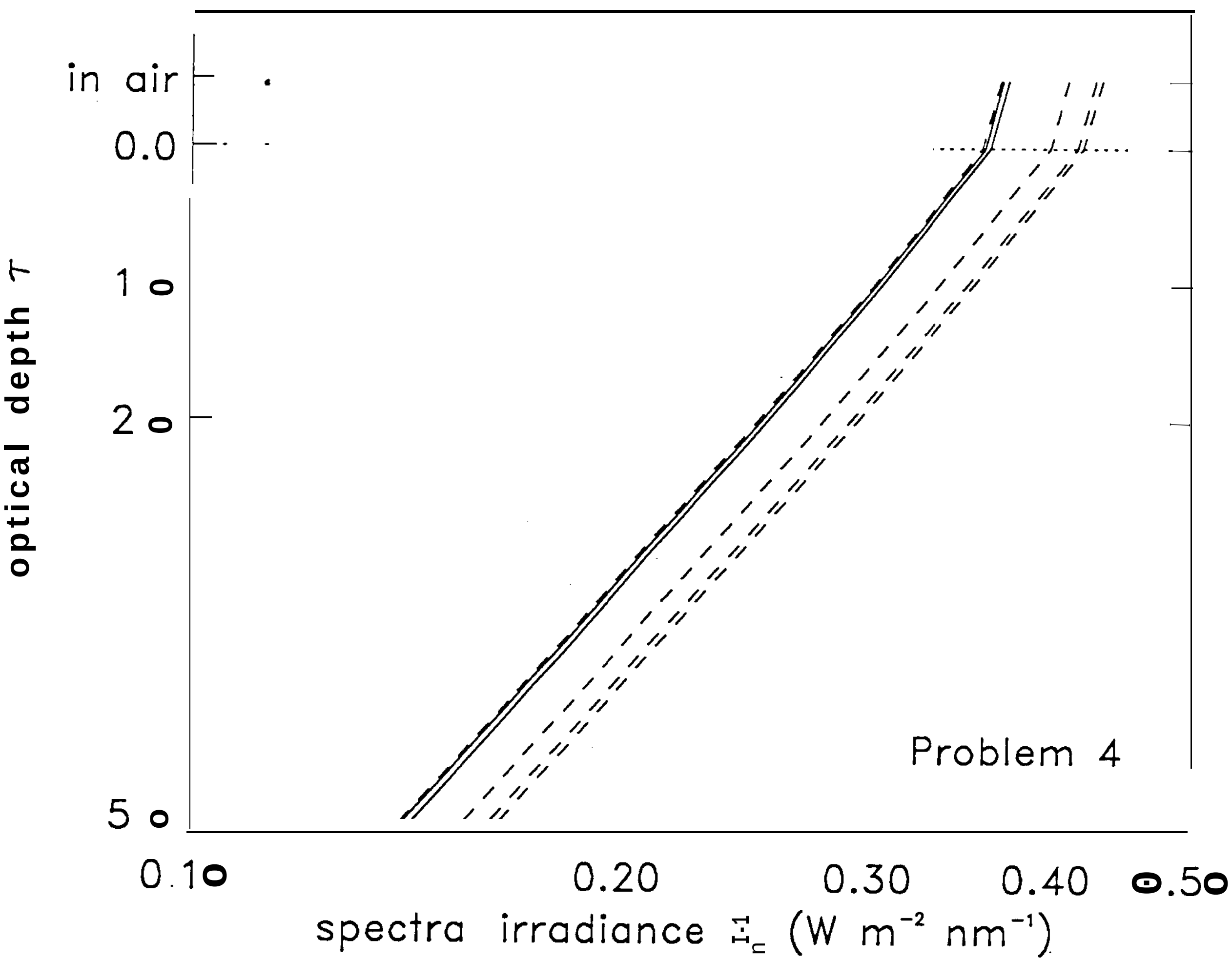
in air
0.0
10
20
50
optical depth τ
Problem 4
0.10
0.20
0.30
0.40
0.50
spectra irradiance E_d (W m^{-2} nm^{-1})

Fig. 5

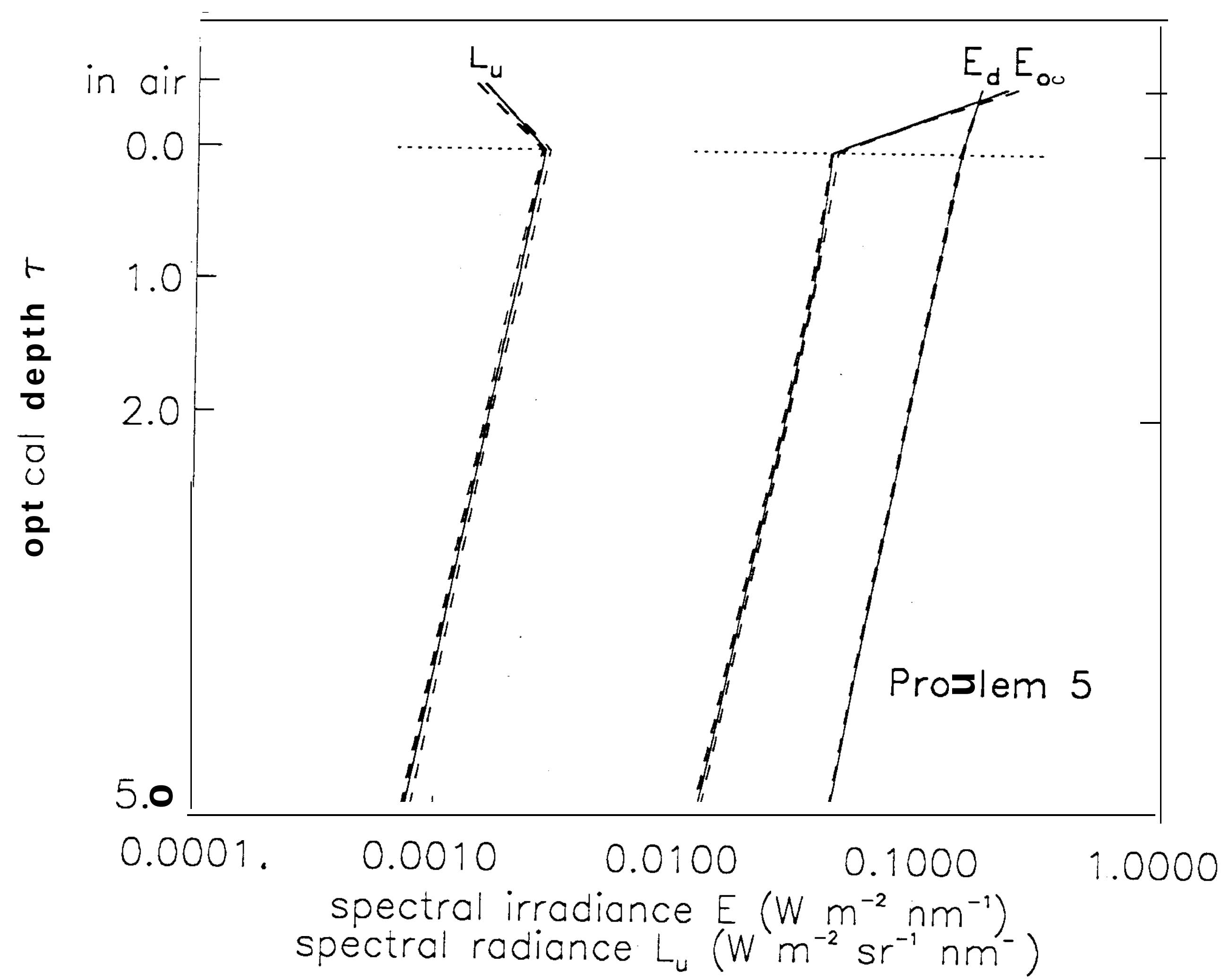

optcal depth τ
in air
0.0
1.0
2.0
5.0
L_u
E_d E_oo
Pro⊐lem 5
0.0001.
0.0010
0.0100
0.1000
1.0000
spectral irradiance E (W m^-2 nm^-1)
spectral radiance L_u (W m^-2 sr^-1 nm^-)

Fig. 6

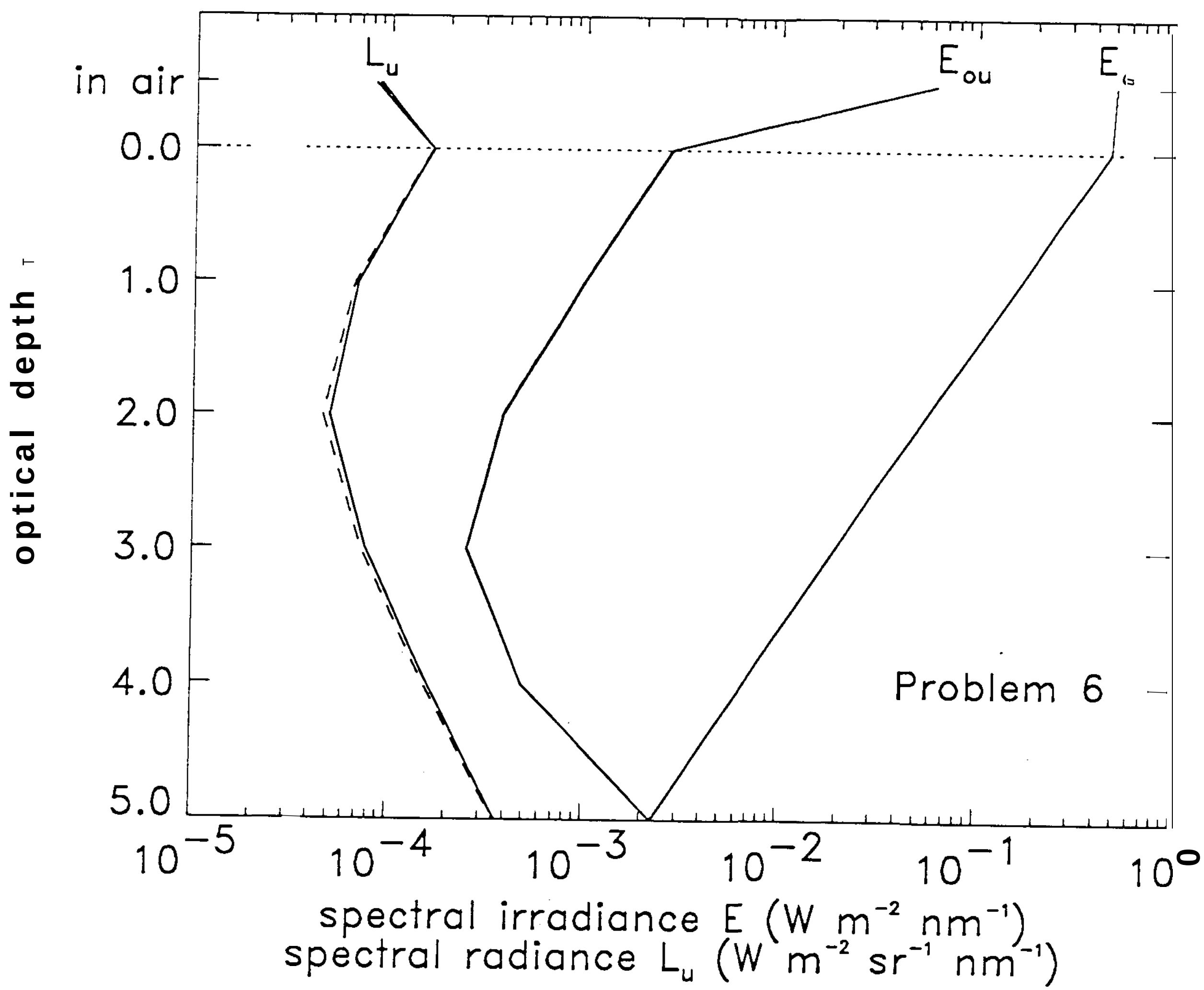

optical depth τ
in air
0.0
1.0
2.0
3.0
4.0
5.0
L_u
E_{ou}
E_o
Problem 6
10^{-5}
10^{-4}
10^{-3}
10^{-2}
10^{-1}
10^{0}
spectral irradiance E (W m^{-2} nm^{-1})
spectral radiance L_u (W m^{-2} sr^{-1} nm^{-1})

Fig. 7

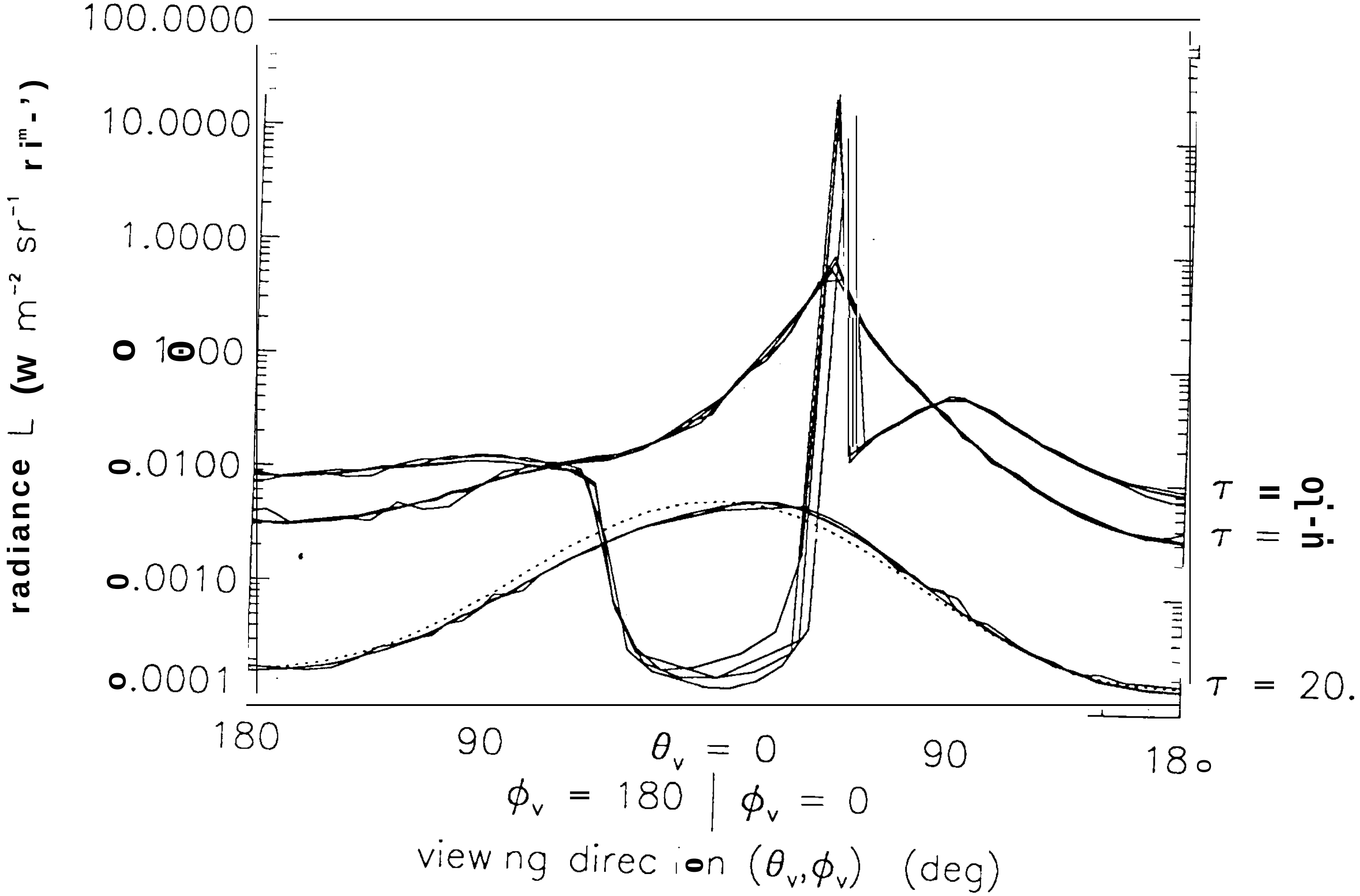

radiance L (W m⁻² sr⁻¹ μm⁻¹)
100.0000
10.0000
1.0000
0.1000
0.0100
0.0010
0.0001
180
90
θv = 0
90
180
φv = 180 | φv = 0
viewing direction (θv,φv) (deg)
τ =
τ =
τ = 20.

Fig 8

Stamnes

to be added to Fig. 8

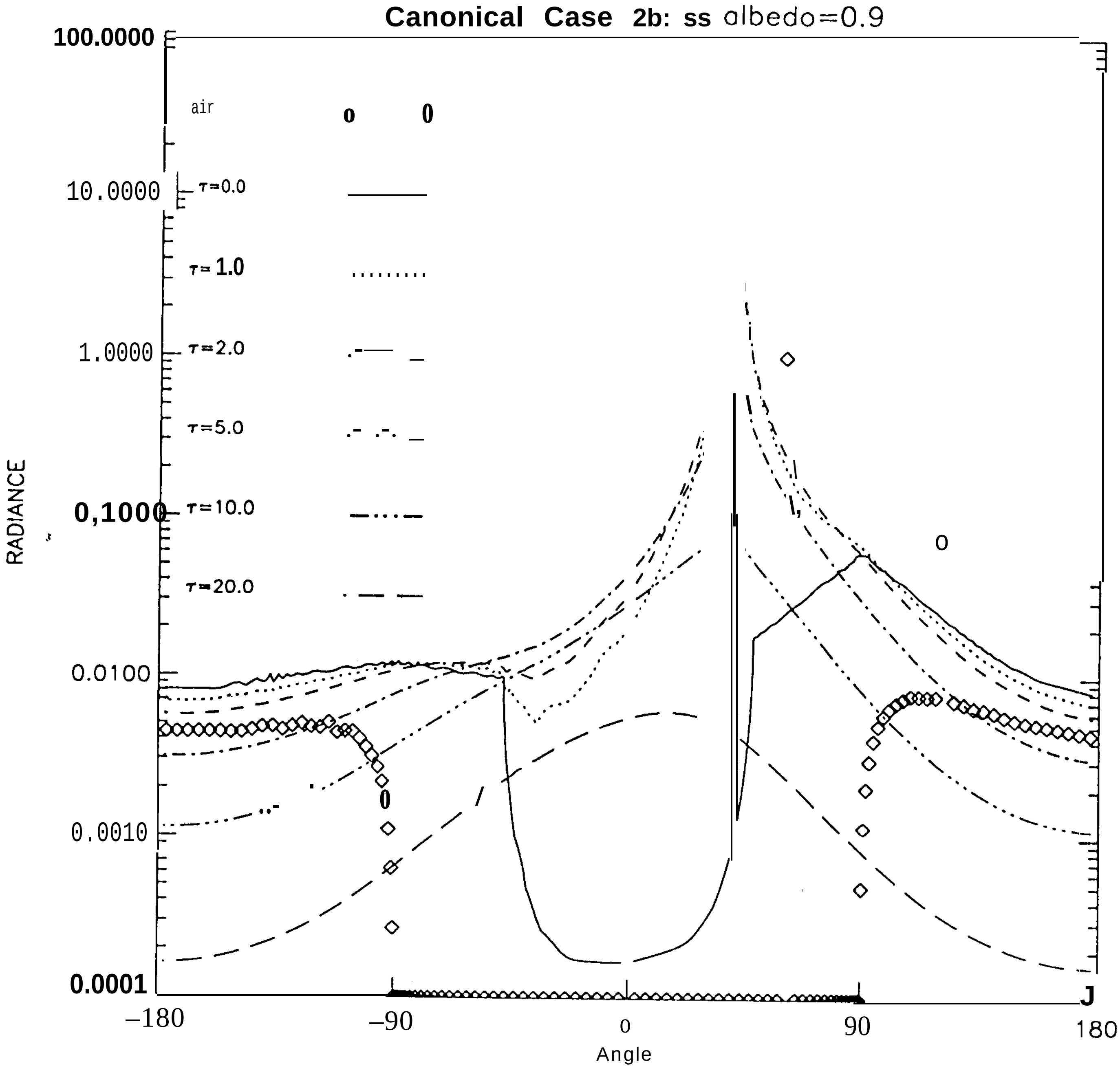

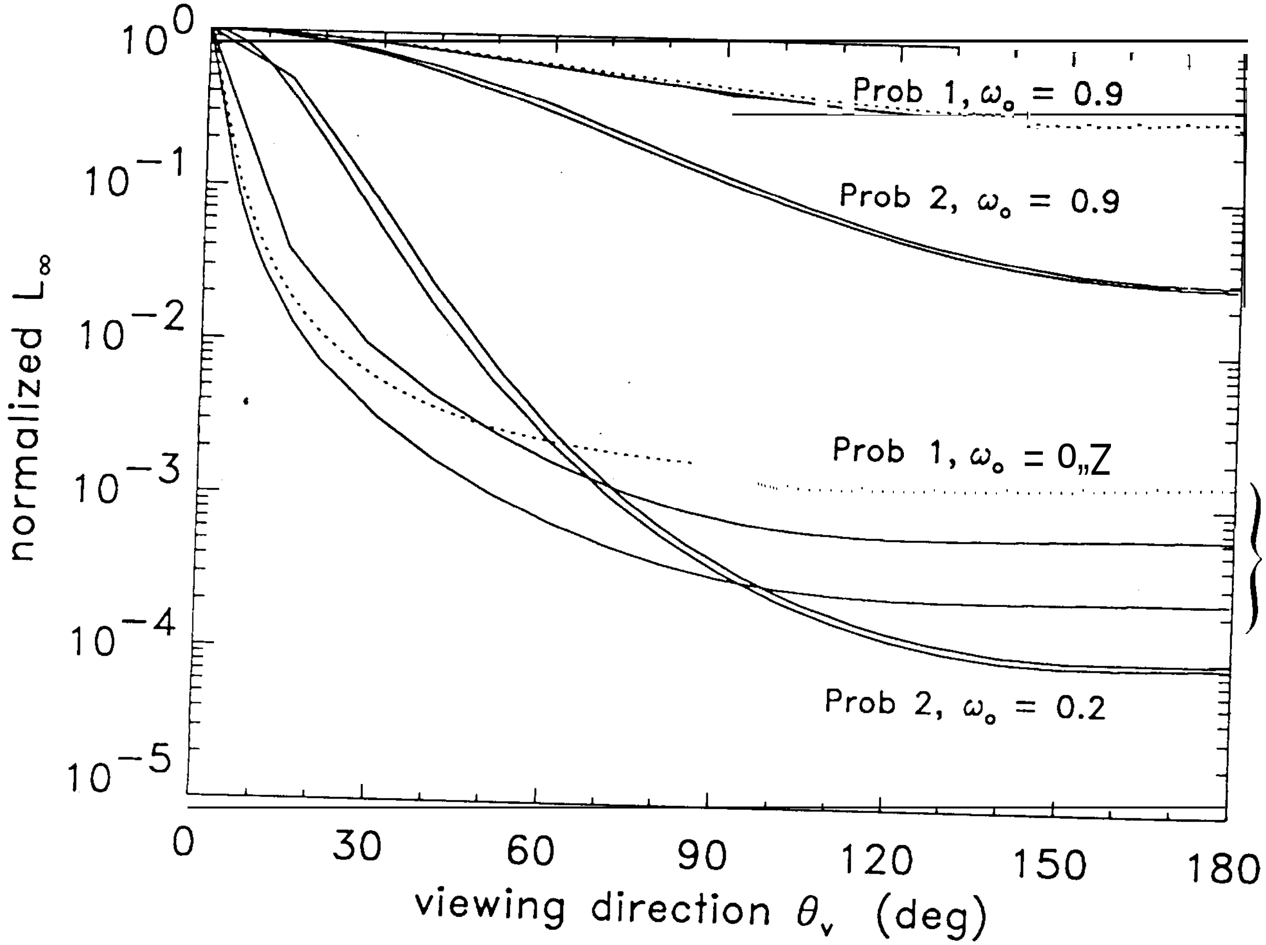

normalized L_∞
10^0
10^{-1}
10^{-2}
10^{-3}
10^{-4}
10^{-5}
Prob 1, ω_o = 0.9
Prob 2, ω_o = 0.9
Prob 1, ω_o = 0„Z
Prob 2, ω_o = 0.2
0
30
60
90
120
150
180
viewing direction θ_v (deg)

Fig. 9